ISSN 2745-3502

Indonesian Applied Physics Letters

Volume 4 No. 2 - December 2023

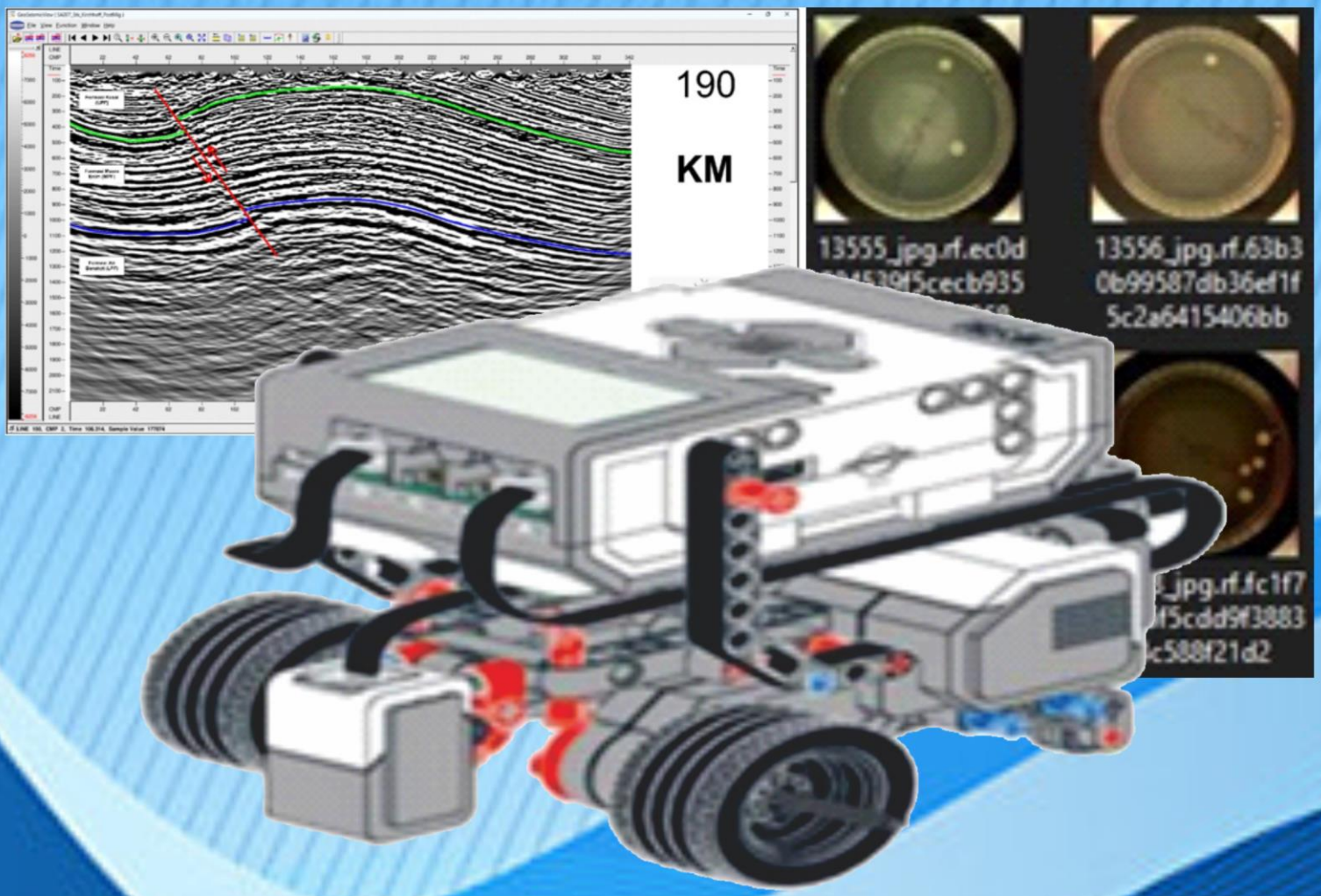

Department of Physics
Faculty of Science and Technology
Universitas Airlangga

CONTENT

Automatic Detection of Escherichia coli Bacteria from Tryptic Soy Agar Image Using Deep Learning Method

Yusril Putra Yonanda[1], Alfian Pramudita Putra[1,2], Endah Purwanti[1,2,a)]

[1] *Biomedical Engineering Study Program, Department of Physics, Faculty of Science and Technology, Universitas Airlangga, Surabaya, Indonesia*
[2] *Biomedical Signals and Systems Research Group, Faculty of Science and Technology, Universitas Airlangga, Surabaya, Indonesia*

[a)] email: endah-p-1@fst.unar.ac.id

Abstract. Escherichia coli is a normal bacterial flora that lives in the human intestine, is harmless and is part of a healthy digestive tract. However, there are several strains of pathogenic Escherichia coli that can cause infections in the digestive tract, namely diarrhea. Diarrheal disease in Indonesia needs treatment and study because most of the diagnoses are still based on clinical diagnosis. Conventional methods used for the detection of Escherichia coli bacteria include culture methods, biochemical tests, and serological tests. This method has the disadvantage of requiring a long time, a large number of samples, and a relatively high error in reading the results. Therefore, the detection process needs to be done automatically using the Faster R-CNN deep learning method. In this research, we used Faster R-CNN with Inception v2 and ResNet-50 architecture and added augmentation and Image Enhancement to the Tryptic Soy Agar image dataset. The test results show that the addition of Image Enhancement greatly affects model performance and the model that has the best performance and is most appropriate to use is the Faster R-CNN ResNet-50 architecture with the addition of Contrast Stretching and Gaussian Filters to the image dataset. This model has 91% accuracy, 90% precision, 95% recall, and 92% F-1 score.

ARTICLE INFO

Article history:

Received: 1 June 2023

Revised: 20 November 2023

Accepted: 21 November 2023

Available online 14 Desember 2023

Keywords:
Escherichia coli,
Automatic Detection,
Deep Learning,
Faster R-CNN.

Cite this as:
Yonanda, Y. P., Putra, A. P., & Purwanti, E. Automatic Detection of Escherichia coli Bacteria from Tryptic Soy Agar Image Using Deep Learning Method. Indonesian Applied Physics Letters, 4(2). https://doi.org/10.20473/iapl.v4i2.46793

Indonesian Applied Physics Letters
e-ISSN: 2745-3502
DOI: 10.20473/iapl.v4i2.46793

INTRODUCTION

Escherichia coli is a normal bacterial flora that lives in the human intestine, is generally harmless, and is part of a healthy digestive tract. However, there are several strains of pathogenic Escherichia coli that can cause infections in the digestive tract such as diarrhea. Infection with pathogenic Escherichia coli bacteria in humans is characterized by a wide range of clinical manifestations ranging from no clinical symptoms or asymptomatic to bloody or bloodless diarrhea (Dutta et al., 2011; Peter et al., 2011). Several factors cause the transmission of Escherichia coli into the human body, including consuming water and food that has been contaminated with Escherichia coli, poor sanitation, and direct transmission from people or animals (Lim et al., 2010).

The World Health Organization (WHO) noted that around 5.6 million children under five died in 2016 and 8.8% were caused by diarrhea (Li et al., 2020). Until now, diarrheal disease in toddlers is still the disease with the second highest mortality rate after pneumonia (Ministry of Health RI, 2020). The Ministry of Health of the Republic of Indonesia has made diarrhea an endemic disease that causes Extraordinary Events (KLB), and reported that diarrhea is a contributor to the mortality rate in children under five in Indonesia. The prevalence of diarrhea in Indonesia, based on the results of Riskesdas (Basic Health Research) in 2018, has decreased by 6.2 percent from Riskesdas in 2013 to 12.3% (Ministry of Health RI, 2018). Even though it has decreased, diarrhea remains the highest cause of infant mortality among other diseases.

Diarrheal disease is still a major problem in Indonesia that needs treatment and study from various aspects because most of the diagnoses made by medical personnel are not based on laboratory examination results but only on clinical diagnosis. For this reason, laboratory tests are very important as a support in examining diarrhea. Several conventional methods are used to determine the presence of pathogenic Escherichia coli bacteria in samples, be it food, drink or in the patient's feces, including culture methods, biochemical tests, and serological tests. This method has the drawbacks of requiring a long time, a large number of samples, and a relatively high error in reading the results (Bakri et al., 2015). In addition, not all Escherichia coli bacteria are present in a sample, for example, Lactobacillus rhamnosus bacteria, which have antioxidant effects that are useful for the digestive tract, and Saccharomyces boulardii bacteria, which have the ability to prevent the formation of wounds in digestive tissue. Because of some of these weaknesses, the detection process must be done automatically. This automatic detection method has many advantages, namely, it can produce accurate, fast, and specific predictions and can be used to overcome the weaknesses of conventional diagnostics.

Automatic detection of pathogenic Escherichia coli bacteria is very important to do to assist doctors in making a diagnosis, one of which is by using machine learning (ML). Research on the automatic detection of Escherichia coli bacteria with ML was carried out by Keeratipibul et al., (2011), which aimed to predict mathematically the relationship between the initial bacterial load, the type of vegetables/fruits, the type and concentration of disinfectants and the residual levels of microorganisms after being sanitized, with application of artificial neural networks (ANN). Escherichia coli and coliform used in this study were isolated from two types of food, and their cultures were activated in Tryptic Soy Broth.

Another study was conducted by Lechowicz et al. (2013) with the aim of classifying Escherichia coli strains in terms of susceptibility/resistance to cephalothin based on 109 Uropathogenic Escherichia coli strains in the infrared spectrum. The data is used to classify E. coli strains using a designed artificial neural network. The result is that the most efficient Artificial Neural Network classifies sensitive/resistant Escherichia coli strains with an error of 5%.

Stocker et al., (2022) evaluated several ML models for predicting Escherichia coli in agricultural pond waters. Escherichia coli concentrations, along with 12 other water quality parameters were measured in water samples. The resulting dataset is used to predict Escherichia coli using the Stochastic Gradient Boosting (SGB) engine, Random Forest (RF), Support Vector Machine (SVM), and the k-nearest Neighbor (kNN) algorithm. The performance results of the model predictions were not significantly different and did not substantially increase the prediction accuracy of the evaluated algorithms.

Based on the performance of ML which is only capable of classifying, a derivative of ML was developed, namely Deep Learning (DL). Programs in DL use more complex capabilities in studying, processing, and also classifying data. (Choi et al., 2020). Convolutional Neural Network (CNN) represents one of the most popular DL algorithms for learning with image and video input. CNN consists of many layers to process and extract data features from the input, which are then used to detect objects (Pal SK, 2018). Region based Convolutional Neural Network (R-CNN) is a form of CNN which was introduced in 2014. R-CNN uses selective search as an external proposal to extract features from the input after being normalized with CNN, which then inputs the output to the classifier to get the results classification and bounding box coordinates as output. R. Girshick & Microsoft Research (2015), solved some of the weaknesses of

R-CNN and built a faster object detection algorithm, namely Fast R-CNN. The approach is similar to the R-CNN algorithm which still uses selective search as an external proposed for building proposal regions, but this is computationally burdensome so the process is slow and affects network performance. Therefore, Ren et al., (2017) developed a Faster R-CNN that replaced the external proposed with the Region Proposal Network (RPN).

Deep Learning successfully reduces the need for feature engineering by leveraging large amounts of data to optimize model parameters and find the most important data features. Tissues trained on data sets are irreplaceable in modern imaging diagnostics. Of course, this does not rule out the possibility in the medical field to help make fast and accurate clinical decisions based on medical procedures. Overall, the application of AI provides innovation for medical technology and diagnostics that enables faster and more efficient medical technologies.

Based on this background, the authors will detect Escherichia coli bacteria in Tryptic Soy Agar images using deep learning, namely Faster R-CNN with Inception v2 architecture, and ResNet-50. The author also adds augmentation and Image Enhancement to the image to improve model performance based on parameters of accuracy, precision, recall, and F1-score.

MATERIALS AND METHOD

Dataset Preparation

Dataset

The data used are images of pathogenic faecal Escherichia coli inoculated onto Tryptic Soy Agar (TSA) plates taken from a journal entitled "AGAR a Microbial Colony Dataset for Deep Learning Detection", by Majchrowska et al., 2021. arXiv:2003.13865v3, which can be accessed from the link https://agar.neurosys.com. The initial step of dataset preparation is selecting a dataset of 510 with the file format (.jpg) in the source.

Anotasi

Annotations are performed on pre-selected image datasets. The annotated dataset will then be randomly divided into a test image dataset of 75 files (15%), and a train image dataset of 435 files (85%). Process annotation, export, and sharing of datasets using the ROBOFLOW service.

Map Labelling

Making a data map label that functions to provide text in the bounding box from the detection results. Writing labels according to the class in the file (.csv) that has been created, and the extension format for creating data map labels is protobuftext (.pbtxt). Making map labels using notepad software.

Data Preprocessing

Resize

The resizing process in this study was carried out to standardize the size of the image dataset. The initial image size, which is 2048×2048, is changed to 600×600. The resizing process in this study was carried out using the ROBOFLOW service.

Brightness Adjustment

Brightness Adjustment is a process of adding and decreasing brightness in datasets in the range of -27% to +27% randomly. Brightness adjustment to the Escherichia coli image dataset was carried out using the ROBOFLOW service.

Contrast Stretching

The first Image Enhancement process is Contrast Stretching or increasing the contrast in the image. The Contrast Stretching process is carried out using the ROBOFLOW service.

Median Filter

The second Image Enhancement stage is the addition of a Median Filter which is a technique that can be used to reduce noise in an image. The process of adding the Median Filter to the Escherichia coli image dataset is carried out using the Google Colaboratory service.

Gaussian Filter

The third Image Enhancement stage is the addition of a Gaussian Filter which is a low pass filter to reduce noise (high-frequency components) by obscuring the image area. The process of adding the Gaussian Filter to the Escherichia coli image dataset is carried out using the Google Colaboratory service.

Training Preparation

This preparatory stage is a step that needs to be done so that the training process can run smoothly. The first step is to install the required libraries in designing the Faster R-CNN system using the TensorFlow framework. The next step is cloning the TensorFlow model repository to facilitate training according to TensorFlow procedures. After the cloning process is complete, it is necessary to create an Environment, which in a programming context is the place where the code will be executed. It includes all executable code and variables available to the code being executed. After the dataset has been uploaded to the environment that has been created, the next step is to create TFRecords so that the model can read the images along with the labels that were created before. TFRecord is a file format that contains images of datasets and the information contained in them. Making a TFRecord is serialized at the data set level, namely one set of records for training, and one set for testing. The input to this TFRecord is the file (.csv) from the train dataset and test dataset, while the output extension format of the generated file is (.record). Faster R-CNN is one of the many architectural models provided by the TensorFlow Object Detection API. The training process is carried out with the Inception v2 and ResNet-50 architectural models that have been trained on the COCO (common objects in context) dataset. The final step is the configuration process which is performed on the file (.config) in the pre-trained model on the previously downloaded COCO Dataset. The file is a configuration that controls the training process. The configuration derived from the pre-trained model needs to be adjusted to the Escherichia coli image dataset.

Training

At this stage, the Faster R-CNN algorithm is designed using Inception v2 and ResNet-50 architecture to be implemented in the detection system on the prepared dataset. The tool used is Google Colaboratory. Model training is carried out using previously adjusted configurations. The end result of the Faster R-CNN training or training process is the formation of a model and records that are ready to be used for detection. After the training process is carried out, a TensorBoard visualization is performed to determine the level of loss during the training stage. The final step is that the Trained model generated from the training process is a file in the form of a checkpoint (.ckpt), while TensorFlow requires a file in the form of protobuf (.pb) so it is necessary to generate a file. The steps taken are to create a frozengraph using the input config file and the resulting checkpoints. The exported file is named “frozen inference graph.pb”.

Testing

The testing phase is used to test dataset testing using a model that has been decorated at the training stage.

Analisis Data

Data analysis was carried out to determine the results of the detection of Escherichia coli bacteria on Tryptic Soy Agar images using Faster R-CNN as shown in Table 1.

TABLE 1. Variasi Kombinasi Model

	Arsitektur	Augmentasi	Preprocessing
RAW DATASET	**Inception v2**	-	-
Model 1	**Inception v2**	*Brightness* ± 27%	*Resize* 600×600 *Contrast Stretching* ***Gaussian Filter***
Model 2	**Inception v2**	*Brightness* ± 27%	*Resize* 600×600 *Contrast Stretching* ***Median Filter***
RAW DATASET	**ResNet-50**	-	-
Model 3	**ResNet-50**	*Brightness* ± 27%	*Resize* 600×600 *Contrast Stretching* ***Gaussian Filter***
Model 4	**ResNet-50**	*Brightness* ± 27%	*Resize* 600×600 *Contrast Stretching* ***Median Filter***

RESULTS

Anotation result

Object annotation is performed using the ROBOFLOW service. The display of the annotation process can be seen in Figure 1. The annotation results from each image will be combined into a *csv file because the TensorFlow Framework can only read files with that extension.

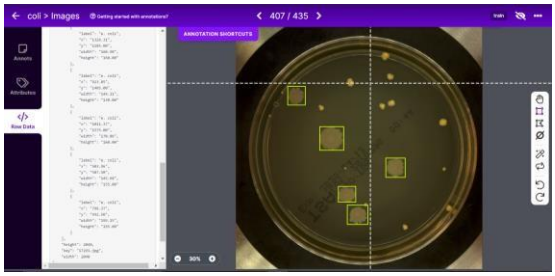

FIGURE 1. ROBOFLOW display

Map Labelling

Label writing is adjusted to the class in the file (.csv) that has been created, and the extension format for creating data map labels is protobuftext (.pbtxt). The process of making a Label Map using Notepad.

Preprocessing Result

Brightness Adjustment result

This study uses decreasing and increasing brightness in the range of ±27% randomly, so that the images will have various characteristics so that they can train better models. The augmentation process is carried out using the ROBOFLOW service

(a) (b)

FIGURE 2. Brightness Adjustment Results (a) Before (b) After

Contrast Stretching

Contrast stretching or contrast enhancement is done because the Escherichia coli image dataset has a slightly low contrast.

(a) (b)

FIGURE 3. Results of the addition of Contrast Stretching (a) Before and (b) After

Median Filter result

The process of adding the Median Filter to the Escherichia coli image dataset is carried out using the Google Colaboratory service

(a) (b)

FIGURE 4. Results of Adding the Median Filter (a) Before and (b) After

Gaussian Filter result

The process of adding the Gaussian Filter to the Escherichia coli image dataset is carried out using the Google Colaboratory service.

(a) (b)

FIGURE 5. The results of adding Gaussian filters (a) before and (b) after

Model Experiment Results

In the training process it will produce a loss which is a value that shows an indication of how bad the predictions of the model are. The model can be said to be perfect if the loss will be zero, otherwise if the model is bad then the amount of loss will be high. The goal for training a model is to train the model to have the lowest possible loss value. The results of the training process are visualized using the TensorFlow feature, namely the TensorBoard, to find out how much the loss rate is. The more the number of steps in the training process, ideally the loss graph will decrease.

Global step/sec

Global step refers to the number of batches or iterations, while global step/sec refers to the number of batches or iterations that can be performed every one second in the training process. Global step refers to the number Based on the graph generated from the TensorBoard Faster R- CNN, the Inception v2 architecture produces an average Global step/sec value of 7.09, higher than the ResNet-50 architecture which produces an average Global step/sec value of 4,3. These results prove that in the training process the Inception v2 architecture model works faster with a speed of 0.141 step/sec when compared to the ResNet-50 architecture model which works with a speed of 0.232 step/sec. Meanwhile, the difference in the addition of image enhancement only has a slight effect on the number of global step/sec.h batches or iterations, while global step/sec refers to the number of batches or iterations that can be performed every one second in the training process.

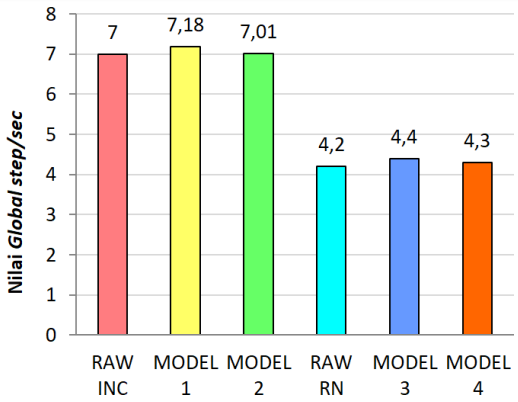

FIGURE 6. Global step/sec results for each model

Classification Loss

Classification Loss is the loss value of the model to classify detected objects into various classes. Based on the graph generated from the TensorBoard, the best Classification Loss value is produced by model 3 which has a value of 0.02 which is a model using image datasets that have been given Image Enhancement in the form of a Gaussian Filter. These results prove that the addition of a Gaussian filter can perform classification with minimal errors when compared to the RAW model.

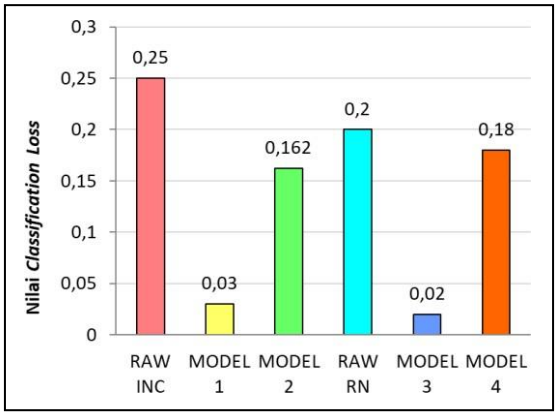

FIGURE 7. Classification Loss results for each model

Localization Loss

Localization loss is also called regression loss which is the error rate of the model to determine the regression box or bounding box containing objects.

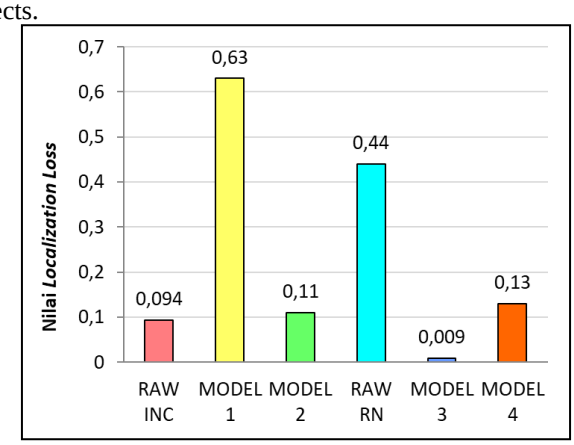

FIGURE 8. Classification Loss results for each model

Results of the Testing Process

The testing process is carried out using a test image dataset of 75 images. This process produces an image that is equipped with a bounding box and labels that have been made before. The image will be analyzed at the data analysis stage to determine the performance of each model.

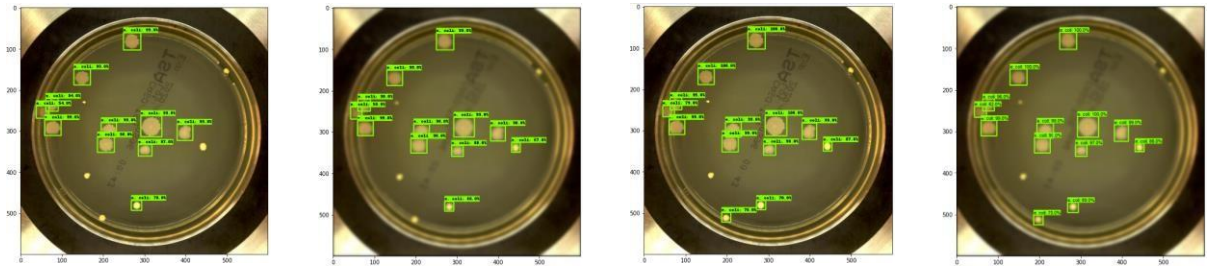

FIGURE 9. The results of the testing process from one of the test images

Model Experiment Analysis

Analysis of the performance of each model using the Confusion Matrix by calculating True Positive, True Negative, False Positive, and False Negative. The calculation of the four components is calculated manually by comparing the ground truth box with the bounding box produced by the model. The Confusion Matrix will tell you how well the model is made. (Nugroho, 2019) True Positive is the success of the system to detect objects as Escherichia coli bacteria, while False Positive is a failure of the system to detect Escherichia coli bacteria so that it will regard other objects as Escherichia coli bacteria. This might be caused by objects that are not Escherichia coli bacteria having similar characteristics to Escherichia coli bacteria so that the system will assume it is correct.

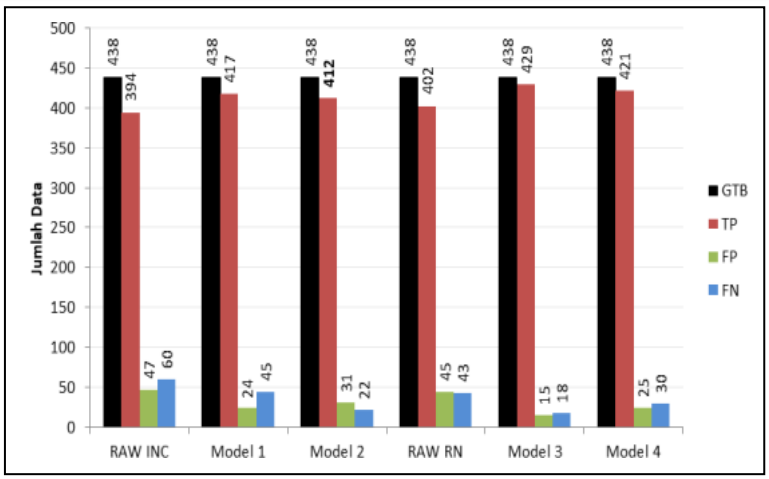

FIGURE 10. Calculation results of the Confusion Matrix Components

True Negative cannot be valuable because in this study only used 1 class, as a result the specificity of the model cannot be calculated. Therefore the performance of the model is determined through accuracy, precision, recall and F1-Score.

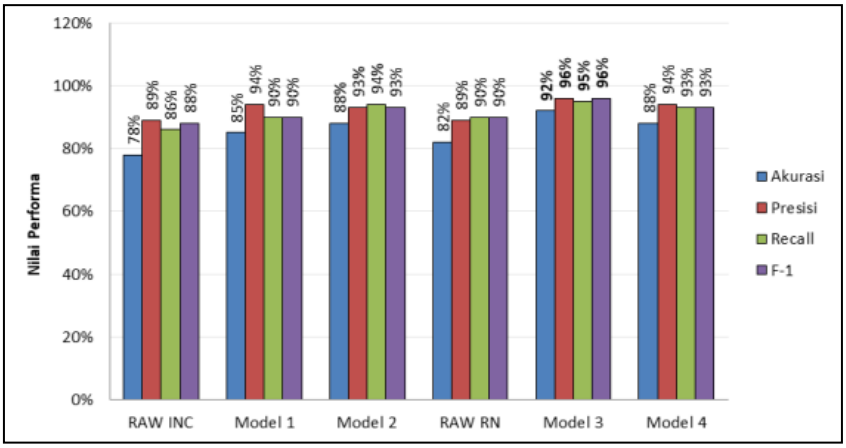

FIGURE 11. Calculation results of the Confusion Matrix Components

Based on the parameters of the table, the model that has the highest Accuracy, Recall, Precision, and F1-Score will be selected. So the most suitable model to be used to detect Escherichia coli bacteria automatically is model 3, namely Faster R-CNN ResNet-50 architecture by adding Image Enhancement in the form of Gaussian Filter to the dataset.

Discussions

The accuracy value is the most important parameter when conducting a study to detect diarrheal disease because True Positive and True Negative are parameters that will be used as a diagnosis for further treatment. If the accuracy value is too low, the model does not have the ability to distinguish between right and wrong objects, so there is no advantage and will cause harm to sufferers. Model 3 has an accuracy value of 92%, so model 3 is the model that has the highest accuracy value among the other models.

The recall value is the second important parameter because it is the value of the comparison between True Positive and all true actual data. In conducting a study on the detection of diarrhea, the appearance of False Negatives was not expected. False negatives or Escherichia coli bacteria that are negatively detected will be detrimental to the patient because it causes the bacteria to be considered as not Escherichia coli bacteria or considered as another object so that the patient will be considered fine by the doctor. The relationship between recall values and False Negatives in equation 2.12 is inversely proportional, so that the fewer the number of False Negatives, the higher the recall value. Model 3 has a recall value of 95%, so model 3 is the model that has the highest recall value among the other models.

The precision value is an important parameter number three because it is the value of the comparison between the True Positive and all the detection results that the model considers true. In accordance with equation 2.11, if there are fewer False Positives, the precision value will be greater. Even if it is a False Positive or other object that is considered to have a large number of Escherichia coli bacteria, it will actually not be detrimental for sufferers of diarrhea because the patient will immediately be given further treatment by a doctor. Model 3 has a precision value of 96%, so model 3 is the model that has the highest precision value among the other models. and recall, which will be used as an option when the difference between the precision and recall values is too great.

CONCLUSION

An object detection model designed using Faster R-CNN with Inception v2 and ResNet-50 architecture has been tested and successfully detects Escherichia coli bacteria in Tryptic Soy Agar images. The addition of Image Enhancement in the form of Median Filter and Gaussian Filter can increase the True Positive value so that it affects the Accuracy and Recall values which are used as important parameters in the detection results of Escherichia coli bacteria in Tryptic Soy Agar images using Faster R-CNN. Faster R-CNN with ResNet-50 architecture has better performance in terms of accuracy, precision, recall, and F1-Score compared to Inception v2 architecture, although Inception v2 architecture has the advantage of being faster in the training process. The most appropriate model for detecting Escherichia coli bacteria in Tryptic Soy Agar images is model 3, namely Faster R-CNN with Res-Net50 architecture with the addition of Image Enhancement in the form of Gaussian Filter which produces 92% accuracy, 96% precision, 95% recall, and F-1 score 96%. F1-Score is a special option if there is an imbalance between False Positive and False Negative in a model. This can result in if the precision value is too high then the recall value will be low, and vice versa. F1-Score is the harmonic mean between precisions.

REFERENCES

1. Bakri, Z., Hatta, M., Massi, M. N. 2015. Deteksi Keberadaan Bakteri Escherichia Coli O157:H7 pada Feses Penderita Diare dengan Metode Kultur Dan PCR, JST Kesehatan. 5 (2), 184 – 192
2. Centers for Disease Control and Prevention. https://www.cdc.gov/ecoli/general/ind ex.html. 2015. Diakses 18 November 2021
3. Chakraborty DB, & Pal SK. 2021. Granular Video Computing: With Rough Sets, Deep Learning and In Iot. World Scientific, Singapore
4. Choi SP, Park YC, Lee JH, Sim SJ, Chang HN. 2012. Effect of L-arginine on Refolding of Lysine-tagged Human Insuline-like Growth Factor 1 Expressed in Escherichia coli. Bioprocess Biosyst Eng. 35: 255-263
5. Choi, R. Y., Coyner, A. S., Kalpathy- Cramer, J., Chiang, M. F., & Campbell, J. P. 2020. Introduction to Machine Learning, Neural Networks, and Deep Learning. Translational Vision Science & Tech, 9 (2), 14
6. Dutta T.K., Roychoudhury S.P., Bandyopadhyay Wani S.A., and I. Hussain. (2011). Detection and characterization of Shiga toxin producing Escherichia coli (STEC) & enteropathogenic Escherichia coli (EPEC) in poultry birds with diarrhea. Indian J. Med. Res. Vol 133, hal: 541-545.
7. El-Melegy M., Mohamed D., & El- Melegy T. 2019. Automatic Detection of Tuberculosis Bacilli from Microscopic Sputum Smear Images Using Faster R-CNN, Transfer Learning and Augmentation, 273
8. Girshick, R & Microsoft Research. 2015. Fast R-CNN, Proceedings of the IEEE International Conference on Computer Vision (ICCV), 1440-1441

9. Girshick, R., Donahue, J., Darrell, T., & Malik J, Rich. 2014. Feature Hierarchies for Accurate Object Detection and Semantic Segmentation, IEEE Conference on Computer Vision and Pattern Recognition, IEEE 2013, 580–587
10. Gonzalez R. C., E. Woods R. B., & R. Masters. 2009. Digital Image Processing, Third Edition, Journal of Biomedical Optics.
11. He K., Zhang X., Ren S., Sun J. 2015. Deep Residual Learning for Image Recognition, Computer Vision and Pattern Recognition
12. Keeratipibul, S., Phewpan, A., Lursinsap, C. 2011. Prediction of Coliforms and Escherichia coli on Tomato Fruits and Lettuce Leaves after Sanitizing by using Artificial Neural Networks, Food Science And Technology, 44, 135
13. Kementerian Kesehatan Republik Indonesia, 2011, Profil Kesehatan Indonesia http://www.depkes.go.id/resources/download/pusdatin/profilkesehatan- indonesia/profil-kesehatanindonesia- 2010.pdf. Diakses 18 November 2011
14. Lechowicz, Ł., Urbaniak, M., Adamus- Białek, A., & Kaca, W. 2013. The Use of Infrared Spectroscopy and Artificial Neural Networks for Detection of Uropathogenic Escherichia Coli Strains' Susceptibility to Cephalothin*, 60 (4), 715-717
15. Lim, J. Y., Yoon, J. W., J, C., & Hovde. 2010. A Brief Overview of Escherichia coli O157:H7 and Its Plasmid O157, Journal of Microbiology and Biotechnology, 20 (1), 1-5
16. Majchrowska, S., Pawłowski, J., Guła, G., Bonus, T., Hanas, A., Loch, A., Pawlak, A., Roszkowiak, J., Golan, T., & Drulis-Kawa, Z. 2021. AGAR a Microbial Colony Dataset for Deep Learning Detection. arXiv: 2108.01234
17. Manning SD. 2010. Deadly Diseases and Epidemics: Escherichia coli Infection, Ed ke-2. New York: Chelsea Publishers
18. Pal SK, Bhoumik D., & Chakraborty DB. 2020. Granulated Deep Learning And Z-Numbers in Motion Detection and Object Recognition, Neural Comput Appl, 32 (21), 16533–16548
19. Pal SK. 2018. Data Science and Technology: Challenges, Opportunities and National Relevance, 14th Annual Convocation Speech, National Institute of Technology, Calicut
20. Peter C.H., Councell F.T., Keys C., and Monday S.R. (2011). Virulence characterization of Shiga-toxigenic Escherichia coli isolates from wholesale produce. Appl. Environ. Microbiol. Vol 77 (1), hal: 343-345.
21. Ren, S., He, S., Girshick, R. B., & Sun, J. 2016. Faster R-CNN: Towards Real- time Object Detection with Region Proposal Networks, IEEE Trans. on Pattern Analysis and Machine Intelligence, 39 (60), 1137-1149
22. Setiawan, A. https://medium.com/data- folks-indonesia/augmentasi-data- pada-computer-vision-45c5ebe10e8f, diakses pada tanggal 15 juni 2022
23. Simonyan, K. & Zisserman, A. 2015. Very Deep Convolutional Networks for Large-Scale Image Recognition. 2-4
24. Sun X., Wu P., Hoi S. C.H. 2018. Face Detection using Deep Learning: An Improved Faster RCNN Approach, Neurocomputing, 299, 43-44
25. Wang, H., Koydemir, H. C., Qiu, Y., Bai, B., Zhang, Y., Jin, Y., Tok, S., Yilmaz, E. C., Gumustekin, E., Rivenson, Y., & Ozcan, A. 2020. Early Detection and Classification of Live Bacteria using Time-lapse Coherent Imaging and Deep Learning, Light: Science & Applications, 9 (118), 3-4
26. Wei, X., Wu Y., Dong F., Zhang J., & Sun S. 2019. Developing an Image Manipulation Detection Algorithm Based on Edge Detection and Faster R-CNN, Symmetry, 11 (1223), 4

Coded Orthogonal Frequency Division Multiplexing Systems: An Overview

Mohammad Farhan[1,a)]

[1]B*aghdad University, Iraq*

[a)] email : mhndfarhan@yahoo.com

Abstract. This article compares the performance of two modulation techniques—quadrature phase shift keying (QPSK) and M-ary quadrature amplitude modulation (M-QAM) with M=8, 16, 32, and 64—in a coded orthogonal frequency division multiplexing system. As an error-correcting code, convolutional technology is employed. A vehicular channel with additive white gaussian noise (AWGN) is utilized for communication. According to simulation data, for QPSK and M-QAM, a coded orthogonal frequency division multiplexing system performs better than an uncoded one. Additionally, the system performs better with QPSK than it does with M-QAM. Additionally, when M rises, the performance declines.

ARTICLE INFO

Article history:

Received: 1 June 2023

Revised: 20 November 2023

Accepted: 21 November 2023

Available online 14 Desember 2023

Keywords:
COFDM,
performance analysis

Cite this as:
Farhan, M. Coded Orthogonal Frequency Division Multiplexing System : An Overview. Indonesian Applied Physics Letters, 4(2). https://doi.org/10.20473/iapl.v4i2.49248

Indonesian Applied Physics Letters
e-ISSN: 2745-3502
DOI: 10.20473/iapl.v4i2.49248

INTRODUCTION

As per the Orthogonal Frequency Division Multiplexing (OFDM) standard, a single high-information rate stream is divided into several lower rate streams that are simultaneously delivered across a number of smaller sub-channels. By carefully selecting subcarrier separating, such as by setting the subcarrier splitting to correspond to the valuable image time frame, it is possible to achieve orthogonality in OFDM. The range of each subcarrier has an invalid at the middle repetition of each of the alternate subcarriers in the framework because the subcarriers are orthogonal.

Since it offers a significant reduction in balancing multi-sided quality compared to conventional correction processes, OFDM has gained more popularity in recent decades. Other interesting elements include combating inter-symbol interference (ISI) and inter-carrier interference (ICI), which causes the receiver's multifarious nature to decline. OFDM offers excellent phantom effectiveness, too. Additionally, OFDM is more resistant to recurrence-specific fading. Numerous recent published works have analyzed the OFDM system due to its exceptional benefits and broad uses [1–7].

A few obstacles exist for OFDM. The main disadvantage is that when the subcarriers are included intelligibly, an OFDM framework with a significant number of sub-carriers has a very high peak-to-average power ratio (PAPR). Furthermore, compared to single-carrier modulated systems, OFDM is more sensitive to Doppler spreading. Additionally, the transmitter and receiver oscillators' defects generate a stage commotion that affects how the framework operates.

The right frequency interleaving and coding are essential in order to take use of the respectable variation that multi-path fading provides. In most OFDM applications, coding thus becomes an integral component. Much study has focused on the appropriate encoder, decoder, and between leaver plan for data transmission using OFDM over fading environments, as in references [8-9]

Despite the fact that a lot of research has focused on the development and use of coded OFDM frameworks for frequency specific fading channels, only a small number of studies provide useful performance analyses of these frameworks because of the unclear nature of this problem. In this case, a frequency-selective quasi-static fading channel is taken into account. This is a logical assumption for an indoor wireless environment that exhibits multi-path fading but eventually exhibits mild alterations, characterized as semi-static. Contrary to coding in Additive White Gaussian Noise (AWGN) channels, where one dominant pair-wise error probability related to the minimum distance of a block code or the free distance of a convolutional code determines the performance of the framework, all pair-wise error probabilities in a fading channel are equal. coded OFDM system decrease as banter polynomial of the sign to-commotion proportion (SNR).Thus the strong association Cherno bound will be excessively free at any extent of SNR when the block length is enormous. Persuaded by the exhibition examination happens on block blurring directs in [10], the arbitrary coding maximum cutoff points [11] and the strong talk cut down limits [12] and moreover the possibility of flitting channel limit are completed for the presentation examination of coded OFDM structure.

COFDM SYSTEM MODEL

The model of COFDM structure is showed up in Fig.1. It is for the most part involving transmitter, recipient, and channel as a transmission way. These three areas are explained in focal points in resulting fragments [2].

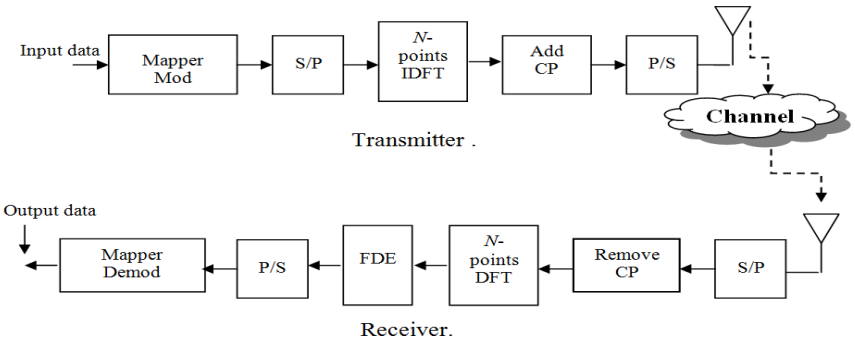

FIGURE 1. Model of COFDM system.

COFDM transmitter

The multi-transporter transmitter involves a game plan of modulators, each with different transporter frequencies. The transmitter by then unites the modulator yields and makes the communicated banner. Expect that the N data to be communicated are, k = 0, 1, . . . , N-1, where is an erratic number in a given quadrature sufficiency modulation(QAM) star grouping . Along these lines, the yield of tweak mapper takes any assessment of sixteen particular assessments of QAM heavenly body showed up in Fig.2 [3], and [4].

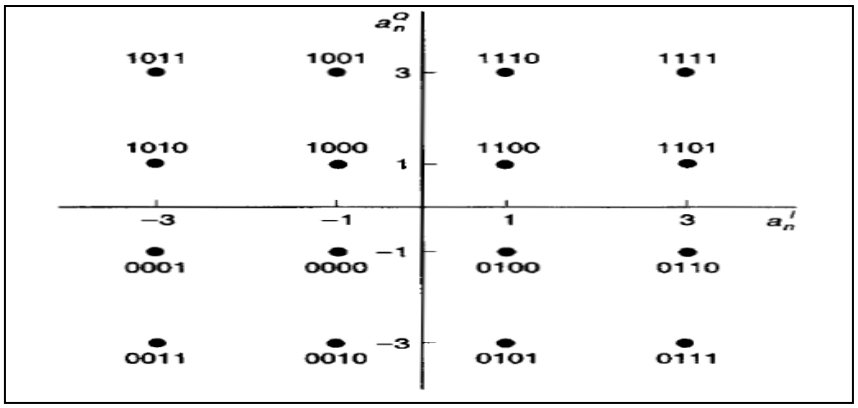

FIGURE 2. 16-ary QAM constellation

The yield from regulation mapper is associated with sequential to resemble (S/P) transformation. The S/P changes over sequential information into N equal streams. In light of the S/P change, the length of transmission time for N images is connected with NTs..Letting t =n, where is the example stretch, the high level multi-transporter transmitter yield is

$$X(nT_s)=\sum_{k=0}^{N-1} x_k\, e^{j2\pi f_k nT_s}$$

Furthermore, if the carrier frequencies are uniformly spaced in the frequency domain by a frequency spacing of f_s,$f_k=kf_s$,k = 0, 1, . . ., N-1,then

$$X(nT_s)=\sum_{k=0}^{N-1} x_k\, e^{j2\pi k f_s nT_s}$$

Equation (1) addresses the result of S/P transformation. Then, the equal information tests are taken care of to the reverse discrete Fourier change (IDFT) block to get the time space OFDM images.

Let $f_s = 1/(NT_s)$ which is the minimum separation to keep orthogonality among signals on different modulators, then the OFDM signal is given by:

$$X(n) =\sum_{k=0}^{N-1} x_k\, e^{j2\pi k(1/N)n}$$

The above recipe is the condition of a N-point IDFT. There are two copies of the got waveform, one on time and the other conceded by some time. ISI is provoked considering the way that the tail some piece of image 1 will intrude with the treatment of image 2. To clear out ISI, a screen timespan is for the most part implanted close to the beginning of each OFDM image [5], [6], and [7].

The cyclic prefix(CP) is a void ISI since it goes about as watch space between moderate images, it similarly change over the straight convolution with channel drive response into a cyclic convolution. As a cyclic convolution in the time space changes over into a scalar expansion in the repeat region, the subcarriers stay symmetrical. The CP is an exact of the last examples of the OFDM image into its front. Allow an opportunity to show the length of CP to the extent that samples,then the extended OFDM images currently have the range of Tsys= Tsub + TG

Fig.3 shows two nonstop OFDM images. The screen interval longer than the best deferral of the multipath channel (thinks about keeping up the symmetry among the subcarriers. As the soundness of each conceded subcarrier has been legitimate by the CP, its symmetry with all unique subcarriers is kept up got done . Exactly when the length of the safeguard interval (CP) is set more limited than the most outrageous delay of a multipath channel, the tail some part of an OFDM image impacts the head some piece of the accompanying image, achieving the ISI.

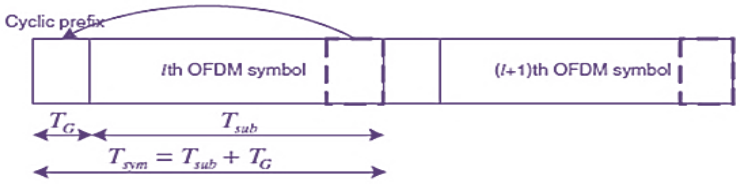

FIGURE 3. OFDM symbols with CP.

The output equation of the CP block is $\overline{x(n)}=x((n-L))_N$, where n = 0, ……, N+L-1. Then the output from the CP block is applied to parallel to serial (P/S) conversion. The P/S converts parallel data into N serial streams [8], and [9].

Convolutional code

A convolutional code is a kind of blunder revising code that produces equality images through the sliding utilization of a boolean polynomial ability to an information stream. The sliding application addresses the 'convolution' of the encoder over the information, which offers climb to the term 'convolutional coding.' The sliding thought of the convolutional codes energizes lattice unraveling using a period invariant lattice. Time invariant lattice translating licenses convolutional codes to be most outrageous likelihood fragile decision decoded with reasonable complexity.

The ability to perform moderate most outrageous greatest probability decision disentangling is one of the critical benefits of convolutional codes. This is rather than exemplary block codes, which are generally addressed by a period variation lattice and in this manner are typically hard-decision decoded. Convolutional codes are consistently depicted by the base code rate and the profundity (or memory) of the encoder [n,k,K]. The base code rate is usually given as n/k, where n is the information rate and k is the result image rate. The profundity is much of the time called the "imperative length" 'K', where the yield is a part of the current information and furthermore the previous K-1 data sources. The profundity may in like manner be given as the amount of memory parts 'v' in the polynomial or the best possible number of states of the encoder (generally 2^v) [9].

Convolutional codes are often portrayed as relentless. Anyway, it could moreover be said that convolutional codes have erratic block length, rather than being steady, since most certifiable convolutional encoding is performed on blocks of information. Convolutionally encoded block codes consistently use end. The inconsistent block length of convolutional codes can moreover be separated to extraordinary block codes, which generally have fixed block lengths that are directed by logarithmic properties.

The code pace of a convolutional code is for the most part changed through image penetrating. For example, a convolutional code with a 'mother' code rate n/k=1/2 may be penetrated to a higher pace of, for example, 7/8 essentially by not sending a piece of code images. The exhibition of a penetrated convolutional code overall scales well with the proportion of equality sent. The ability to perform saving fragile decision translating on convolutional codes, and what's more the block length and code rate versatility of convolutional codes, spreads the word about them very well for advanced correspondences [10].

Communication channel

To simplify the mathematical analysis, a time-invariant channel is assumed which has the following response with R taps

$$h^T = [h_0\, h_1 \ldots . h_{R-1}]$$

The channel impulse response is circularly convolved with the transmitted signals owing to the CP in OFDM signals, so the output of the channel will be as follows

$$y(n)=h(n)* \overline{x(n)} + N(n)$$

$$y(n)=h(n)* x\big((n-L)\big)_N + N(n)$$

$$y(n)=h(n)x(n)+N(n)$$

The output of the channel (i.e. the received signal) can be written in matrix form as follows [10]:

$$Y \quad \begin{bmatrix} \overbrace{0 \cdots 0}^{N_t-R+1} & h_{R-1} & h_{R-2} & \cdots & h_0 & \overbrace{0 & & & \cdots & 0}^{N-1} \\ 0 \cdots & 0 & h_{R-1} & h_{R-2} & \cdots & h_0 & & & \cdots & 0 \\ & & & & \cdots & & & & & \\ 0 & & & & \cdots & 0 & h_{R-1} & h_{R-2} & \cdots & h_0 \end{bmatrix} \quad = X + N$$

COFDM receiver

At the receiver end, firstly, the received signal is applied to S/P conversion. The S/P converts serial data into parallel streams. Then the received signals $Y=[\, y_0\ y_1 \ldots . y_{N-1}\ ]^T$ after removal of the CP can be expressed as:

$$Y = \begin{bmatrix} h_0 & 0 & \cdots & & & 0 & h_{R-1} & h_{R-2} & \cdots & h_1 \\ h_1 & h_0 & 0 & & & \cdots & 0 & h_{R-1} & \cdots & h_2 \\ & & & & & \cdots & & & & \\ h_{R-1} & h_{R-2} & \cdots & h_0 & 0 & & & & \cdots & 0 \\ 0 & h_{R-1} & \cdots & h_1 & h_0 & & & & \cdots & 0 \\ & & & & & \cdots & & & & \\ 0 & \cdots & & & 0 & h_{R-1} & & & \cdots & h_0 \end{bmatrix} \begin{bmatrix} x_0 \\ x_1 \\ \cdot \\ \cdot \\ \cdot \\ x_{N-1} \end{bmatrix} \mathrm{N}$$

$$Y = QX + N$$

where x consists of the last N elements in X and N is the Gaussian noise. Note that the circulant matrix Q can be diagonalized by the DFT and IDFT matrices, yielding

$$Q = F^{-1}\mathrm{H}F$$

where F andF^(-1) are the DFT and IDFT matrices, respectively. The matrix H is a diagonal matrix:

$$\mathbf{H} = \begin{bmatrix} H_0 & 0 & \cdots & 0 \\ 0 & H_1 & \cdots & 0 \\ & \vdots & & \\ 0 & \cdots & 0 & H_{N-1} \end{bmatrix}$$

where every askew component relates to the recurrence space channel reaction at the comparing subcarrier.

Note that OFDM changes over the convolution in time region into expansion in recurrence area and subsequently fundamental one-tap recurrence space balancers can be used to recover the sent images. After DFT, images are demodulated and decoded to procure the communicated information bits by demodulation mapper[11-14].

SIMULATION RESULTS

Maltlab 2017 is used to mimic the COFDM system, with modulation methods like QPSK, 8-QAM, 16-QAM, 32-QAM, and 64-QAM. Convolutional code is integrated with the model with the intention of enhancing the framework's execution; as a result, the OFDM is referred to as coded OFDM (COFDM). It is decided to use a convolutional code with an octal generating polynomial of length 7 (133,171). Vehicle channel with 11 ways is the channel display in use. Table 1 contains a list of the reproduction-related parameters.

TABLE 1. COFDM Simulation Parameters.

Parameter	Value
FFT Size	512
Cyclic Prefix Length	20Samples
Time between Samples	24.41 ns
Channel Coding	Convolution Code with Rate=1/2
Modulation Types	QPSK, 8-QAM, 16-QAM, 32-QAM, and 64-QAM
Channel Model	Vehicular Channel with 11Paths

Bit-error-rate (BER) vs signal-to-noise ratio (SNR) measurements are used to assess how well the overall system is working. The execution of the framework for an uncoded system is shown in Figures 4 and 5, respectively. It appears that a coded system performs better than an uncoded system. Additionally, QPSK performs better than M-QAM, and the performance declines as M grows.

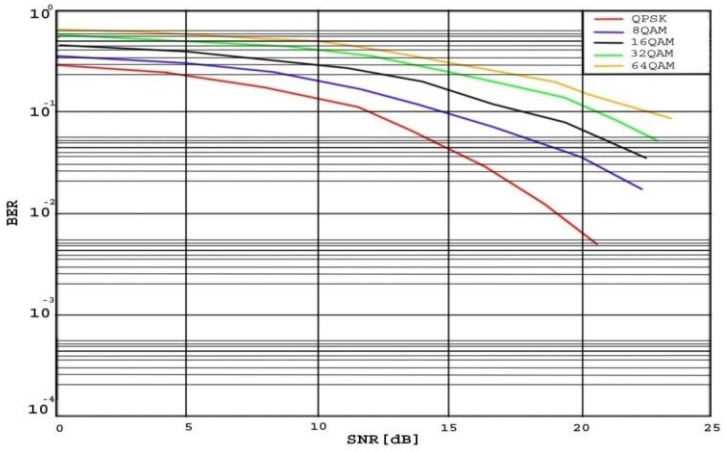

FIGURE 4. BER performance of un-coded OFDM over multipath fading channel.

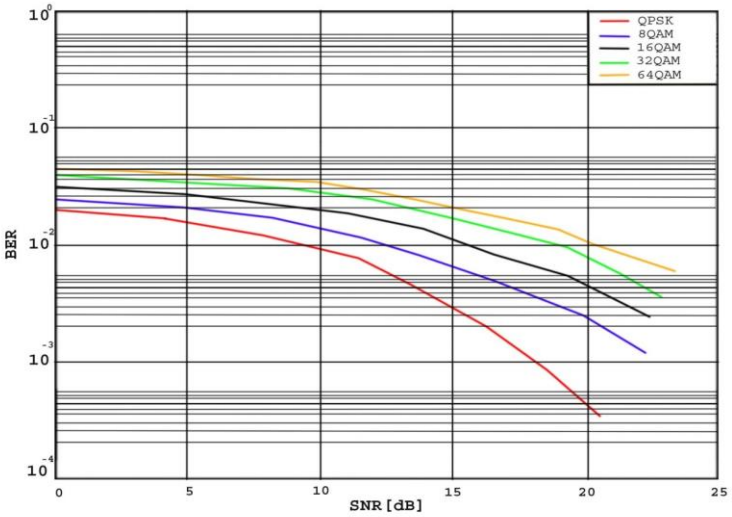

FIGURE 5. BER performance of COFDM over multipath fading channel.

CONCLUSION

To investigate the performance of the COFDM system over the vehicular channel with AWGN utilizing QPSK, 8-QAM, 16-QAM, 32-QAM, and 64-QAM, a model of the system was created. As an error-correcting code, convolutional technology was employed. The outcomes demonstrate that COFDM performs better than un-coded one. Additionally, QPSK offers superior performance than M-QAM. Additionally, the performance suffers as M increases.

REFERENCES

1. J. Bingham, “Multicarrier Modulation for Data Transmission: An Idea Whose Time Has Come,” IEEE Commun. Mag., vol. 2, no. 5, May, 1990, pp. 5–14.
2. B. LeFloch, M. Alard, and C. Berrou “Coded Orthogonal Frequency Division Multiplex,” Proc. IEEE, vol. 83, June, 1995, pp. 982–96.
3. B. Stephen, “History of OFDM,” IEEE Commun. Mag.,vol. 47, no. 11,Nov., 2009, pp. 26–35.
4. V. Sharma, “BER performance of OFDM-BPSK,-QPSK,- QAM over AWGN channel using forward Error correcting code,” International Journal of Engineering Research and Applications, vol. 2, issue 3, 2012, pp.1619-1624.
5. Y. Khan, “To Improve Performance of OFDM System Using Optimize Adaptive Coding Technique with Convolutional and BCH Coding,” International Journal of Application or Innovation in Engineering & Management, vol. 3, issue 5, May 2014.
6. B. Alex,“Behavior and Techniques for Improving Performance of OFDM Systems for Wireless communications,” International Journal of Advanced Research in Computer and Communication Engineering vol. 4, issue 1, January 2015.
7. Sachin, “Analyzing the BER Performance of OFDM-System with QPSK and BPSK Modulation Technique,” International Journal of Innovative Research in Advanced Engineering, vol. 2. no.6, 2015.
8. B. Lu, X. Wang, and K. R. Narayanan, “LDPC-based space-time coded OFDMsystems over correlated fading channels: Performance analysis and receiver design,” IEEE Trans. Wireless Commun., vol. 1, pp. 213-225, 2002.
9. H. Kim, "Turbo coded orthogonal frequency division multiplexing for digitalaudio broadcasting," in 2000 IEEE Intern. Confer. on Commun., vol. 1, pp. 420-424.
10. E. Malkamaki and H. Leib, " Coded diversity on block-fading channels," IEEE Trans. Inform. Theory, vol. 45, pp. 771-781, 1999.
11. R. G. Gallager, Information Theory and Reliable communication. New York, Wiley, 1968.

12. S. Arimoto, "On the converse to the coding theorem for discrete memoryless channels," IEEE Personal Commun., vol. IT-19, pp. 357-359, 1973.
13. N Al-Awad, and M. Al-Rawi" On the Performance of COFDM System," International Journal of Open Information Technologies, vol.6, pp.39-42, 2018.
14. M. Liu, W. Shen, J. Yan and H. Zeng, "A Simulation Method of Orthogonal Frequency Division Multiplexing," 2022 14th International Conference on Computer Research and Development (ICCRD), Shenzhen, China,, pp. 388-393, 2022.

APPLICATION OF SURFACE CONSISTENT AMPLITUDE CORRECTION (SCAC) IN THE "HRNR" FIELD

Hafid Rizki Nur Rohman[1] and Yatini[1*)]

[1] *Geophysical Engineering, Faculty of Mineral Technology, University of Pembangunan Nasional Veteran Yogyakarta*

Jl. SWK Jl. Ring Road Utara No.104, Ngropoh, Condongcatur, Kec. Depok
Kabupaten Sleman, Daerah Istimewa Yogyakarta 55283
Indonesia

[*)]Corresponding author: jeng_tini@upnyk.ac.id

Abstract. This research aims to enhance the quality of 3D onshore seismic data and understand subsurface structures in a study area. We implemented the Surface Consistent Amplitude Correction (SCAC) method in seismic data processing. This study's results demonstrate that using SCAC significantly improves the quality of seismic data amplitudes, especially in eliminating previously disruptive noise in the analysis. Following the application of SCAC, seismic data amplitudes become clearer and stronger. The interpretation of the enhanced seismic data with SCAC revealed the presence of a significant geological structure, namely a reverse fault, which has significant implications for subsurface understanding. The location of this reverse fault was identified at inline 190 within the CMP range of 60 to 120, with time domain depths ranging from 150 ms to 1250 ms in the southwestern part of the cross-section. This research highlights that SCAC plays a key role in enhancing seismic data resolution and enables the identification of reverse faults that were previously challenging to discern. These findings make a crucial contribution to understanding subsurface geology in the study area and hold significant potential in the context of natural resource exploration. This study firmly establishes that SCAC is an effective tool in improving seismic data quality and revealing important geological structures, especially reverse faults, which can be a primary focus in subsurface geological studies in this research area.

ARTICLE INFO

Article history:

Received: 1 June 2023

Revised: 20 November 2023

Accepted: 21 November 2023

Available online 14 December 2023

Keywords:
Seismic Data Processing,
Seismic Reflection,
3D Land Seismic Data,
SCAC.

Cite this as:
Yatini, Y., & Nur Rohman, H. R. . An APPLICATION OF SURFACE CONSISTENT AMPLITUDE CORRECTION (SCAC) IN THE "HRNR" FIELD. Indonesian Applied Physics Letters, 4(2). https://doi.org/10.20473/iapl.v4i2.49910

Indonesian Applied Physics Letters
e-ISSN: 2745-3502
DOI: 10.20473/iapl.v4i2.49910

INTRODUCTION

Seismic reflection processing typically consists of several steps or sequences, and one of the conventional seismic processing stages is deconvolution and migration. Deconvolution is a stage that applies deconvolution functions to seismic data to improve resolution by carefully removing system frequencies (Sheriff and Geldart, 1995). Conversely, migration is a stage in seismic processing that aims to restore dipping reflectors to their original time positions and eliminate diffraction effects resulting from specific structures, thereby enhancing spatial resolution and the subsurface seismic image quality (Yilmaz, 2000).

Conventional and unconventional seismic processing methods are employed in seismic reflection processing. Conventional seismic reflection processing typically focuses on denoising or noise removal from seismic data without specific approaches in its application. In contrast, unconventional processing methods follow steps similar to conventional processing but incorporate additional enhancements to improve seismic data quality without excessively removing existing seismic signals, thereby minimizing data loss during processing. Standard modules used in unconventional seismic data processing include Surface Consistent Amplitude Correction, Surface Consistent Deconvolution, Coherent Noise Attenuation, Wild Amplitude Attenuation, and several others. This study applies an unconventional method by adding Surface Consistent Amplitude Correction (SCAC). The purpose of implementing the Surface Consistent Amplitude Correction (SCAC) module is to maintain the consistency of seismic data amplitudes and enhance seismic data resolution for more accurate subsurface interpretation. Additionally, the unconventional method applied in this study aims to preserve more amplitudes, typically lost due to Spherical Divergence effects (Sheriff & Geldart, 1995).

The field research "HRNR" is conducted to assess the impact of Surface Consistent Amplitude Correction on the quality of seismic data and subsurface structural analysis. The initial step involves implementing Surface Consistent Amplitude Correction in the seismic data. The results of this implementation will be evaluated by considering improvements in resolution and the level of detail in the geological structure images that can be obtained from the "EPS-107" seismic data. Thus, this research aims to understand the effects and the success of Surface Consistent Amplitude Correction in enhancing the quality of seismic data and improving the existing structural patterns in the research area.

Geology

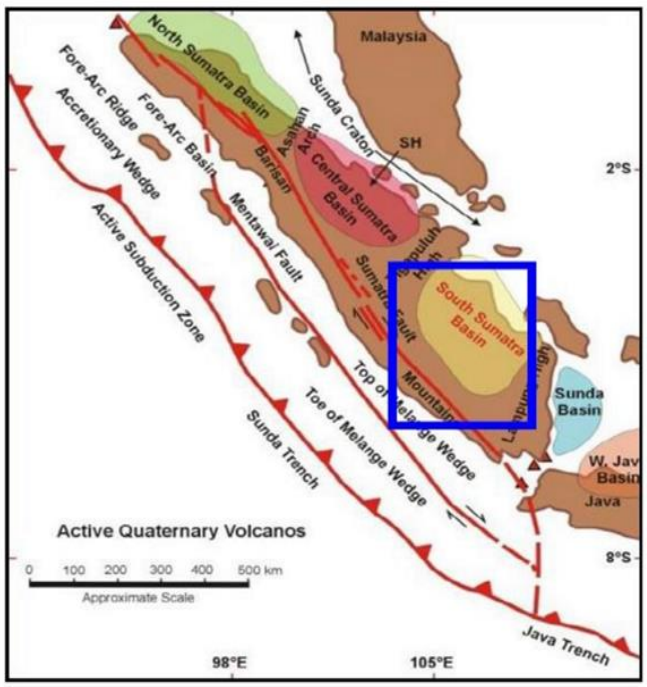

Figure 1. The Geographical Location of The South Sumatra Basin (De Coster, 1974).

The South Sumatra Basin depicted in Figure 1 is a Tertiary basin located in the southwestern part of Sumatra. The Semangko Fault and the Bukit Barisan Range are to the southwest, the Sunda Shelf is to the northeast, the Lampung Highlands is

to the southeast, and the Twelve Mountains and Thirty Mountains are to the northwest bound this region. This basin is formed as a result of the interaction between the Sunda Shelf (as a part of the Asian continental plate) and the Indian Ocean plate, covering an area of approximately 330 x 510 km2, and falls into the category of foreland or back-arc basins. The South Sumatra Basin is also recognized as one of the most prolific hydrocarbon-producing basins off the eastern coast of Sumatra in Indonesia (Blake, 1989; Wisnu & Nazirman, 1997; Panggabean & Santy, 2012).

Stratigraphy

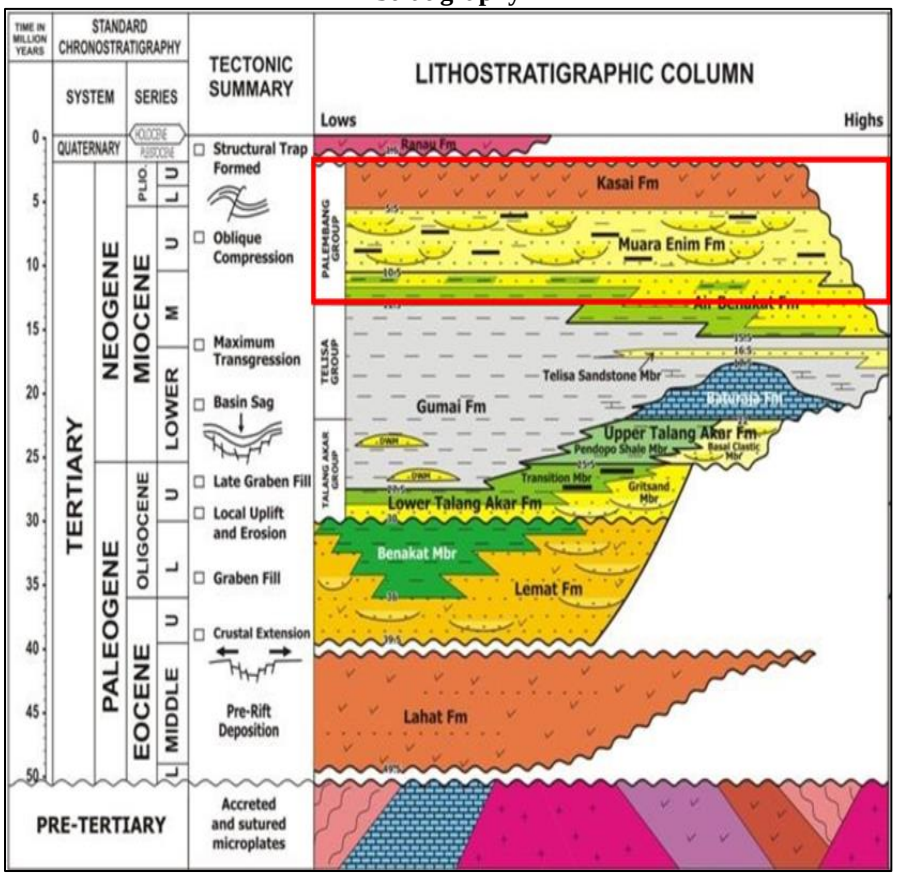

Figure 2. Regional Stratigraphic Column of the South Sumatra Basin (Kamal et al., 2005)

The HRNR Field has a geological stratigraphy comprising three distinct formations, as indicated in Figure 2, marked in red boxes. These stratigraphic units represent sedimentary sequences deposited during different geological time intervals, each characterized by its unique rock layers and characteristics (Kamal et al., 2005). The division of these formations is as follows:

1. Upper Palembang Formation (Kasai):

   The Lower Palembang Formation represents rock layers deposited during the initial phase of a regression cycle in the HRNR Field. The composition of this formation includes glauconitic sandstone, claystone, shale, and carbonate-bearing sandstone. This indicates lithological variations encompassing both clastic and carbonate sediments. The formation dates back to the Middle Miocene and was formed in a shallow marine environment. Depositional processes occurred in shallow waters, suggesting that the marine environment at that time was relatively close to sea level. This formation provides valuable insights into the paleoenvironment and sea-level changes during the Middle Miocene in the HRNR Field (Kamal et al., 2005).
2. Middle Palembang Formation (Muara Enim):

   The Middle Palembang Formation, or Muara Enim Formation, consists of sandstone, claystone, and coal layers in the HRNR Field. In the southern part of the basin, the lower boundary of this formation is marked by coal layers often used as markers. Its thickness varies from approximately 1500 to 2500 feet (about 450 to 750 meters). This formation ranges in age from Late Miocene to Pliocene and was deposited in shallow marine, delta plain, and non-marine environments (Kamal et al., 2005).
3. Lower Palembang Formation (Air Benakat):

   The Kasai Formation is the youngest geological formation in the South Sumatra Basin. It was formed during the orogenic period in the Plio-Pleistocene timeframe. The formation process occurred through erosion from the Barisan and Tiga Puluh Mountains. The Kasai Formation consists of tuffaceous sandstone, clay, shale, and thin coal layers. While

the exact age of this formation cannot be precisely determined, it is believed to have a Plio-Pleistocene age. Deposition of this formation occurred in a terrestrial environment (Kamal et al., 2005).

RESEARCH METHODOLOGY

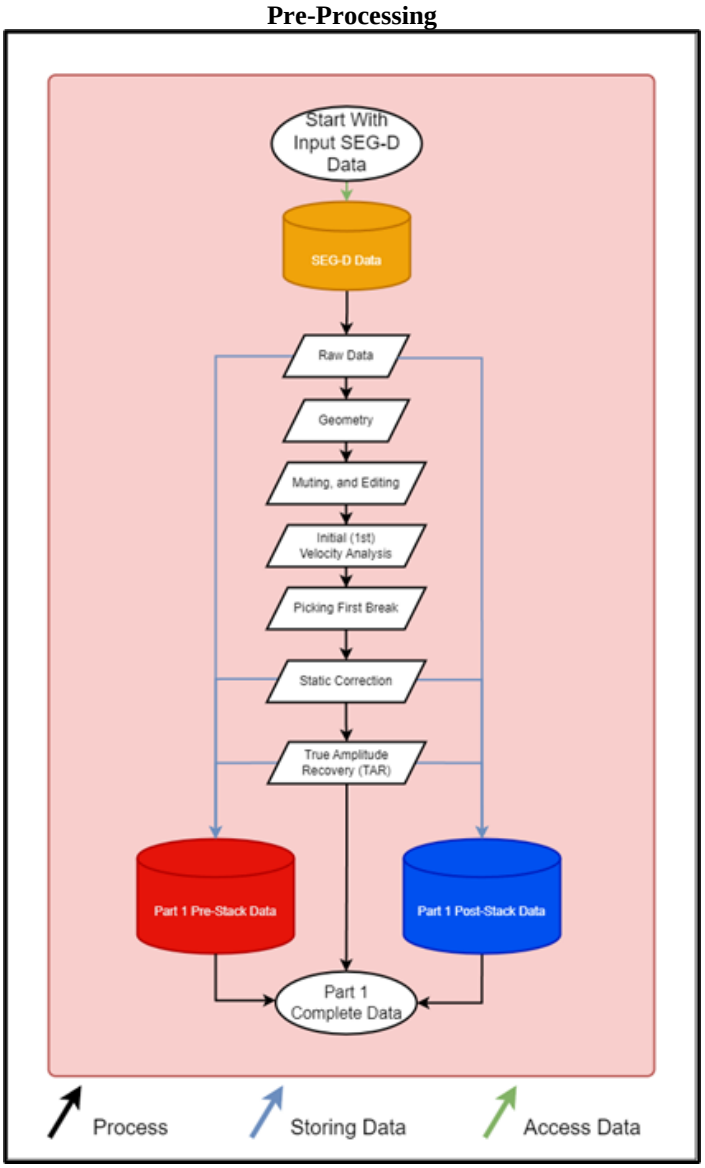

Figure 3. Pre-Processing Stage

The first stage is the pre-processing stage in Figure 3. This stage aims to prepare seismic data before further analysis is conducted. These steps include initial noise removal and correction for amplitude imbalances in the data. By preparing this data, the quality of the seismic recordings to be processed in the next stage becomes better and more accurate. The data required at this stage is the raw or secondary data in the research area, resulting in pre-processed data.

Processing

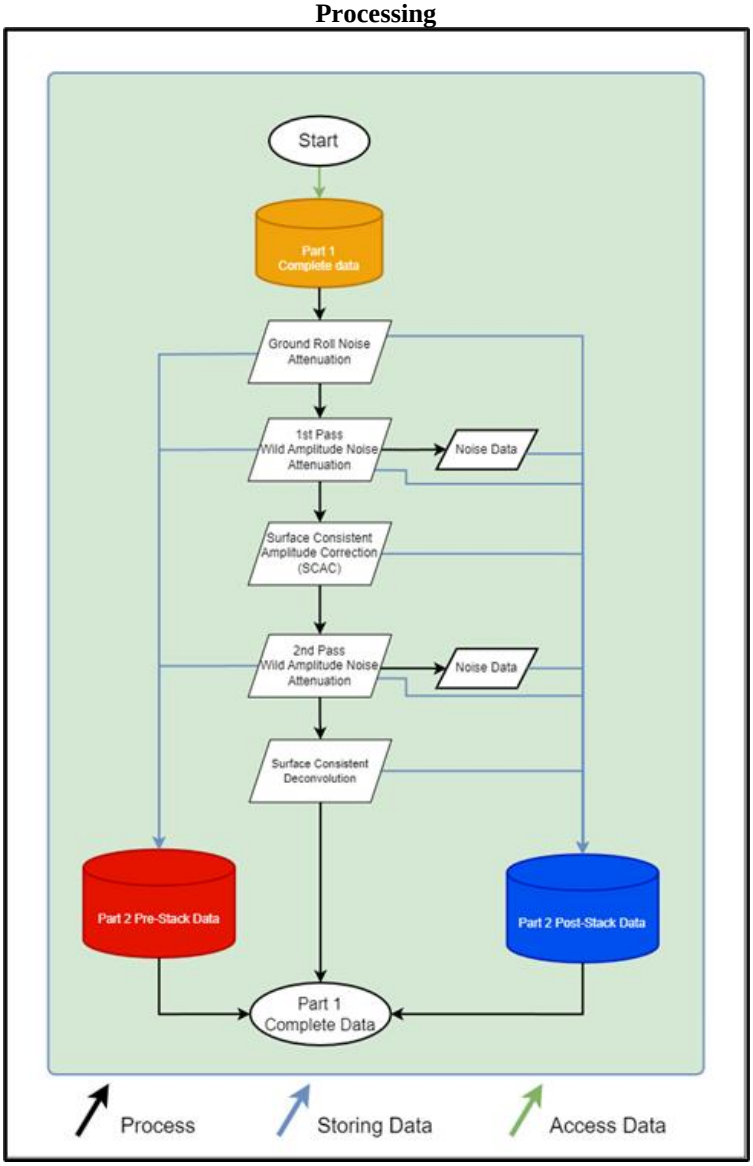

Figure 4. Processing Stage

The second stage is the processing stage in Figure 4. In this stage, the primary focus is removing the noise in the initial seismic data. This processing is done without amplitude compensation. The result is cleaner seismic data free from disturbances that may have occurred during acquisition. By reducing seismic noise in this stage, subsurface information can be more clearly revealed. In the Processing stage, the input data used is the data that has undergone pre-processing, which will then undergo denoising or the removal of seismic data noise present in the research area, resulting in seismic data ready for the post-processing stage.

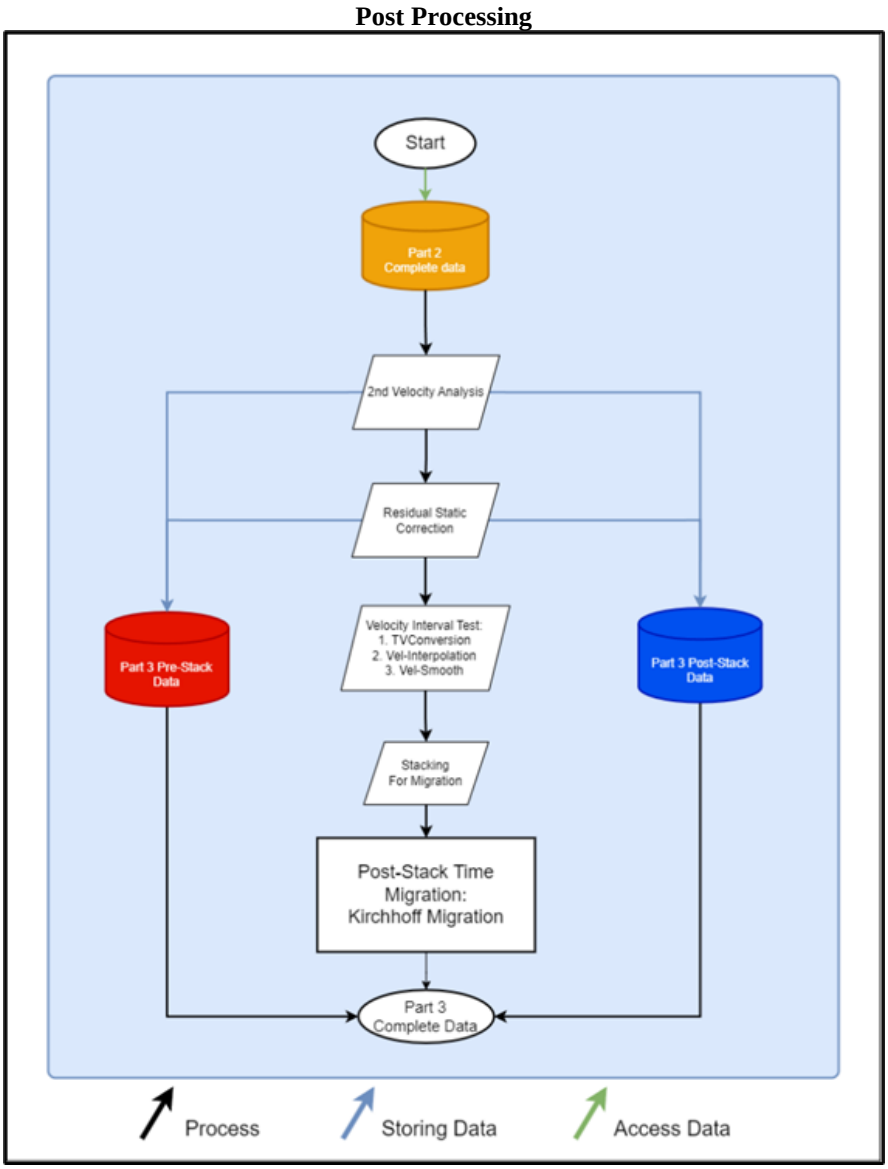

Figure 5. Post-Processing Stage

The third stage, the post-processing stage in Figure 5, involves advanced processes in removing seismic noise. This time, it is done with consideration for amplitude compensation. The goal is to optimize seismic data by highlighting residual seismic noise. The input for the post-processing stage is seismic data that has already undergone denoising or the removal of seismic noise such as ground roll noise, wild noise, and other unwanted noise sources. In this stage, the seismic data may still be ambiguous due to factors from the earlier deconvolution, so residual static correction is needed to restore the amplitude positions to their original state. Subsequently, migration is applied to the seismic data to reposition the reflector points within the seismic data, resulting in both preserved and unpreserved amplitudes.

Interpretation

The interpretation of seismic data involves two main approaches: qualitative and quantitative interpretation in Figure 5. In qualitative interpretation, the emphasis is placed on observing amplitude patterns within the data. Through this analysis, the primary goal is to explain how these amplitude patterns can indicate the presence of geological formation boundaries and faults. For example, when we observe wave patterns that show zones with higher reflection levels in Seismic Reflection data, this can be interpreted as a sign of the presence of specific rock layers, such as sand or limestone, with different geological properties (Sheriff, R. E., & Geldart, L. P., 1995).

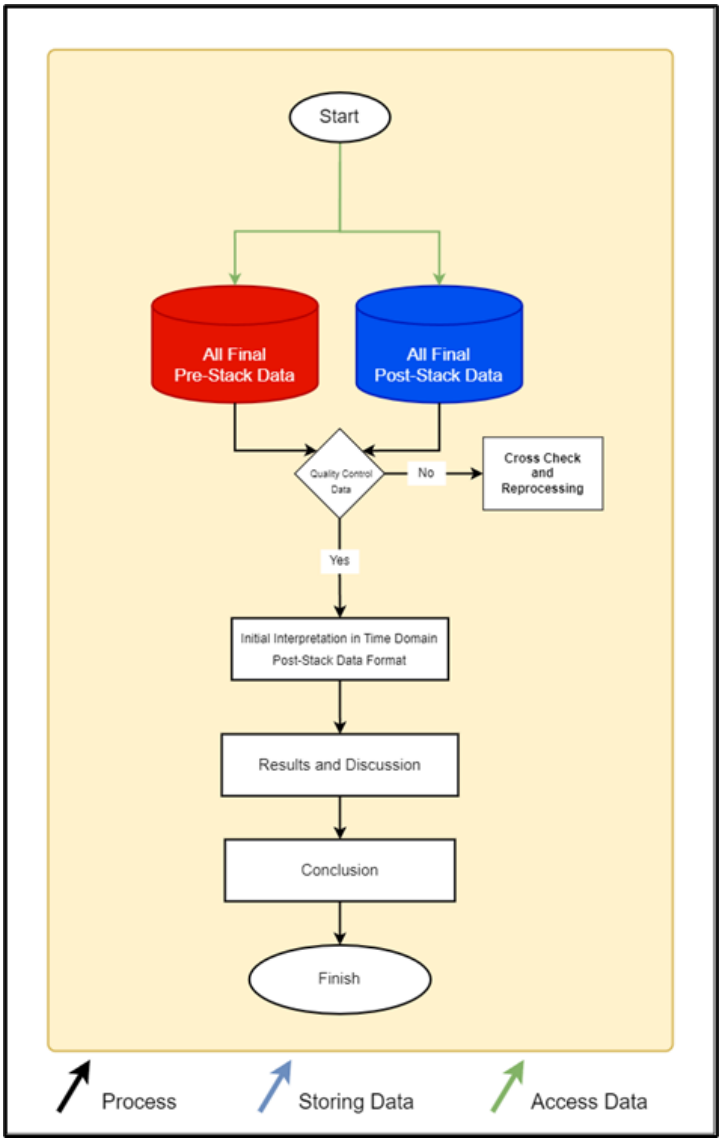

Figure 6. Interpretation Stage

The interpretation of seismic data involves two main approaches: qualitative interpretation and quantitative interpretation, as shown in Figure 6. In qualitative interpretation, the emphasis is placed on observing amplitude patterns within the data. Through this analysis, the primary goal is to explain how these amplitude patterns can indicate the presence of geological formation boundaries and faults. For example, when we observe wave patterns that show zones with higher reflection levels in Seismic Reflection data, this can be interpreted as a sign of the presence of specific rock layers, such as sand or limestone, with different geological properties (Sheriff, R. E., & Geldart, L. P., 1995).

RESULT AND DISCUSSION

Results of Applying Surface Consistent Amplitude Correction (SCAC)

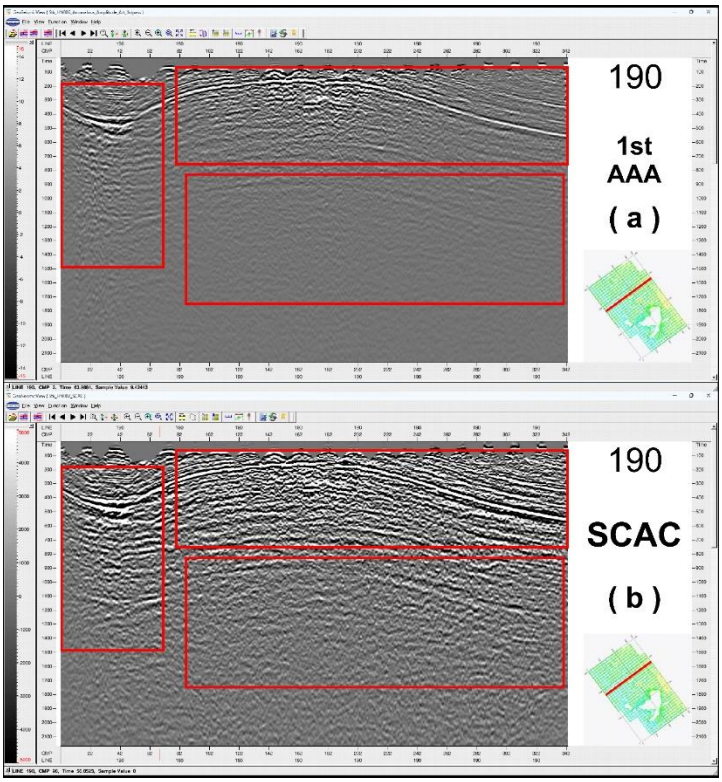

Figure 7. Results of Applying Surface Consistent Amplitude Correction (SCAC)

Table 1. Comparison Between Non-SCAC and SCAC

Comparison	Non-SCAC	SCAC
Seismic Data	Only visible down to a depth of time 600 Clearly visible down to a depth of time 2100	Clearly visible down to a depth of time 2100
Noise	Only slightly visible (wild noise) due to lower resolution factors More visible (wild noise) due to higher resolution factors compared to non-SCAC	More visible (wild noise) due to higher resolution factors compared to non-SCAC
Vertical Resolution	The boundary between the Muara Enim formation and the Benakat water is not clearly visible boundary between the Muara Enim formation and the Benakat water	The clearly visible boundary between the Muara Enim formation and the Benakat water
Horizontal Resolution	The boundary layer between the Muara Enim formation and the Benakat water appears to vanish and lacks continuity The disappearing boundary layer between the Muara Enim formation and the Benakat water becomes visible and exhibits continuity	The disappearing boundary layer between the Muara Enim formation and the Benakat water becomes visible and exhibits continuity

Structure Pattern	Appears not to be a fault body, but rather appears as cracks due to unclear vertical and horizontal resolution factors Cracks that appear as faults in non-SCAC show vertical displacement (upthrust) due to unclear vertical and horizontal resolution factors.	Amplitudes that appear as cracks in non-SCAC show vertical displacement (upthrust) due to unclear vertical and horizontal resolution factors.

In Figure 7, part (a) depicts a portion of seismic data on inline 190 before the application of surface consistent amplitude correction. Therefore, part (b) illustrates the seismic section on inline 190 after applying surface consistent amplitude correction to the seismic data. In the red boxes, CMP 1 to 68 at a time depth of 180 ms to 1480 ms, CMP 80 to 342 at a time depth of 50 ms to 750 ms, and CMP 85 to CMP 342 at a time depth of 800 ms to 1750 ms show that the amplitudes, which initially appeared weak in Figure (7a), become stronger Figure (7b). This enhancement or strengthening aids in analyzing and improving the noise distribution in the seismic data within the research area, which was not eliminated during the 1st AAA stage and can be further cleaned in the 2nd AAA stage. There can be multiple interpretations during the surface consistent amplitude correction stage, marked by the red boxes on CMP 1 to 68. In part (a), inline 190 appears to be a basin. Still, after the migration stage, as shown in Figure 8, which is the result of the interpretation of the cross-section, it is indicated that the portion from CMP 1 to 68 is suspected to be a part of a reverse fault, commonly referred to as an uplifted fault, located beneath the surface. The analysis based on Figure 5 can be summarized in Table 1.

Results of Applying Migration

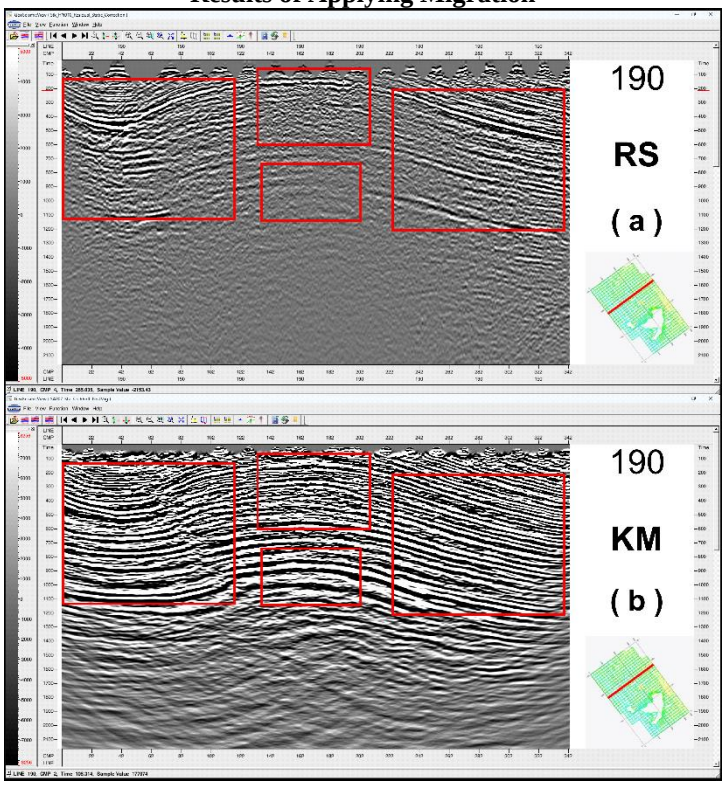

Figure 8. Inline 190 (a) Residual Static Correction Vs (b) Migration.

Referring to Figure 6, there are cross-sections for inline 190 (left) and a cross-line section (right), consisting of (a) a section that has not yet been subjected to the Migration module or has already undergone Residual Static Correction module, and (b) a section resulting from the application of seismic Migration. In the red boxes, significant changes in amplitude patterns can be observed as a result of the Migration application, specifically in CMP 1 to 118 at a time depth of 130 to 1130 ms, CMP 130 to 208 at a time depth of 50 to 600 ms, and CMP 133 to 202 at a time depth of

700 to 1112 ms. These changes indicate clear shifts in the locations of seismic wave reflector points, making the cross-sections generated during the migration stage ready for interpretation in the time domain.

Results of Interpretation

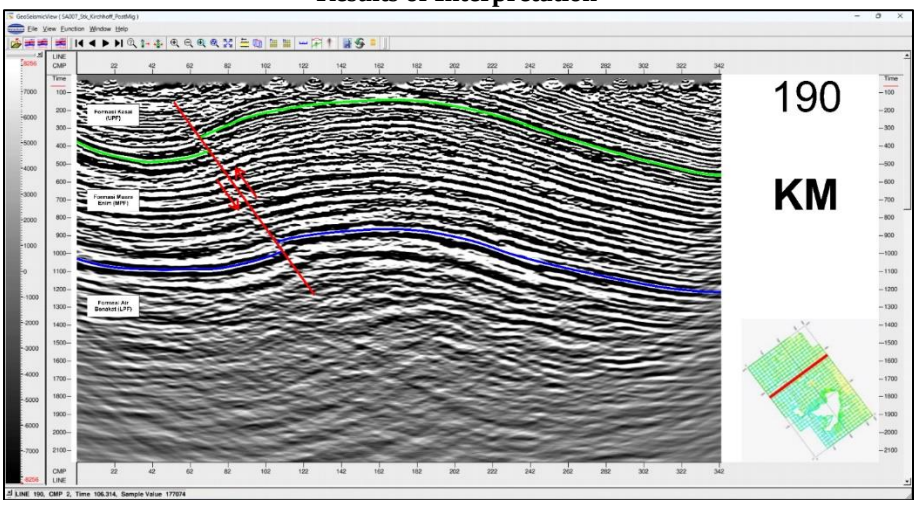

Figure 9. Interpretation of Inline 190 Cross-Section.

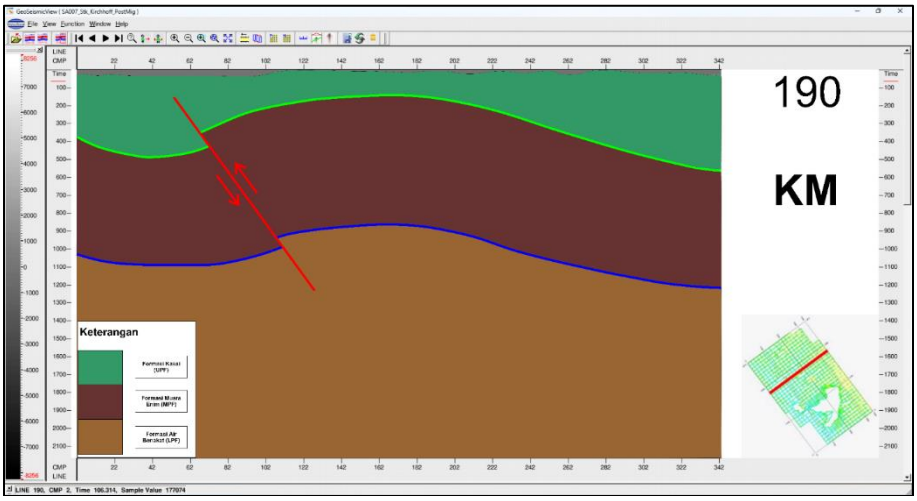

Figure 10. Inline 190 (a) Subsurface Model of Inline 190 Cross-Section.

In Figure 7 and 8, we can observe the interpretation of the seismic cross-section in line 190. This interpretation is based on local stratigraphic knowledge in the research area, which consists of three formations in ascending order: the Kasai Formation, the Muara Enim Formation, and the Air Benakat Formation. This interpretation provides a deeper understanding of the subsurface structure in the research area. Based on the interpretation in the time domain, the green horizon is interpreted as the boundary between the Kasai Formation and the Muara Enim Formation, while the blue horizon is interpreted as the boundary between the Muara Enim Formation and the Air Benakat Formation. Based on this information, the research area meets the criteria for a petroleum system.

The Kasai Formation is interpreted as the caprock or sealing rock in this study, as the rocks in the Kasai Formation tend to have relatively low permeability, making them suitable for a caprock. Next is the Muara Enim Formation, which is interpreted as the reservoir in this study because it exhibits sufficient porosity, particularly due to the presence of sandstone in this formation. The Air Benakat Formation is interpreted as the source rock in this study due to the organic content within this formation.

One significant finding in this interpretation is the presence of a reverse or uplifted fault in the research area. This fault is located in the CMP range of 60 to 120 on the cross-section and has a time depth ranging from 150 ms to 1250 ms in the southwestern part of the cross-section. This reverse fault indicates past geological movement in the research

area. Specifically, a reverse fault is a type of fault that experiences vertical movement where one block of rock is pushed upward and over another block. The interim formation model can be seen in Figure 8

CONCLUSION

Based on the research objectives, several significant conclusions can be drawn from the results of this study. Firstly, Surface Consistent Amplitude Correction (SCAC) has a noteworthy impact on seismic data quality. Secondly, its influence on subsurface structural analysis is pivotal, particularly in detecting reverse faults, which signify significant past tectonic activity and have important implications for fluid storage and movement within rock formations. Thirdly, the effective application of SCAC hinges on the thoughtful selection of appropriate parameters and settings. Finally, SCAC successfully enhances the resolution and detail of geological structure images in seismic data, facilitating interpretation by making horizons, formation boundaries, and reverse faults more discernible.

ACKNOWLEDGMENTS

The author thanks the Geophysical Engineering Department of the University of Pembangunan Nasional Veteran Yogyakarta, SKK MIGAS, PT. BGP Indonesia, and all parties involved.

REFERENCES

1. Blake, C. (1989). Tertiary Basins of Thailand. In Proceedings of the Symposium on Stratigraphic Correlation of Southeast Asia, 1988 (pp. 291-299). Geological Society of Malaysia.
2. Wisnu, W. S., & Nazirman, M. (1997). Structural styles in the South Sumatra basin, Indonesia. Indonesian Petroleum Association, Proceedings of the Twenty-Fourth Annual Convention, Vol. 1, 421-441.
3. Panggabean, H., & Santy, L. D. (2012). Sejarah Penimbunan Cekungan Sumatera Selatan Dan Implikasinya Terhadap Waktu Generasi Hidrokarbon. Jurnal Sumber Daya Geologi, 22..
4. Kamal, A. (2005). Structural and stratigraphic framework of the South Sumatra Basin. In Proceedings of the Indonesian Petroleum Association, 30th Annual Convention (pp. 185-199).
5. Yilmaz, O. and Doherty, S.M. (2000) Seismic Data Analysis: Processing, Inversion, and Interpretation of Seismic Data. Society of Exploration Geophysicists, Tulsa, 2027 p.
6. Sherif, R.E. dan Geldart, L.P., 1995, Exploration Seismology Second Edition, Cambridge University Press, New York USA.

Design of Digital Control System for Line Following Robot

Mohanad Abdulhamid [1)]

[1]*Al-hikma University, Iraq*

[a)] email : moh1hamid@yahoo.com

Abstract. Design of mobile robots has become an increasingly growing trend in the technology of modern times. They are very attractive engineering systems, not only because of many interesting theoretical aspects concerning kinematics, intelligent behavior and autonomy, but also because of applicability in many human activities. A typical example is the line following robot (LFR). In order for a LFR to function effectively, it must demonstrate excellent line tracking control. This is achieved by having accurate and responsive control algorithms as well as high precision color sensor systems. This paper proposes a system to show that good line tracking performance can be achieved with moderately simple digital control algorithms. The platform used is a differentially driven wheeled robot constructed using the Lego Mindstorms components. The simulation models are presented and analyzed using MATLAB Simulink . The main programming environment is the EV3 Software.

ARTICLE INFO

Article history:

Received: 1 June 2023

Revised: 20 November 2023

Accepted: 21 November 2023

Available online 14 December 2023

Keywords:
Digital control,
line following robot

Cite this as:
Abdulhamid, M. Design of Digital Control System for Line Following Robot . Indonesian Applied Physics Letters, 4(2). https://doi.org/10.20473/iapl.v4i2.48729

Indonesian Applied Physics Letters
e-ISSN: 2745-3502
DOI: 10.20473/iapl.v4i2.48729

INTRODUCTION

Robotics is a branch of engineering that involves the conception, design, manufacture and operation of robots. The field overlaps with electronics, computer science, artificial intelligence, mechatronics, nanotechnology, bioengineering and control engineering. Robots are mechatronic engineering products, capable of acting autonomously while implementing assigned behaviors in various physical environments. The developed use of robots in many areas makes the fundamental understanding of them fundamental.

In recent years there has been a rapid increase in the use of digital controllers in control system. It has become routinely practicable to design very complicated digital controllers and to carry out the extensive calculations required for their design. The current adoption of digital rather than analog control in robotics is due to the genuine advantages found in working with digital signals rather than continuous time signals.

The use of analog controllers in control engineering poses problems such as limited accuracy, susceptibility to noise and drift of power supply, cost ineffectiveness and less flexibility. Digital control systems are more suitable for modern control systems because of reduced cost, noise immunity and speed.

Line following robots need to adapt accurately, faster, efficiently and cheaply to changing operating conditions. The drawbacks prominent in analog controllers reduce their suitability in robotics. Hence, the necessity for digital controllers which provide better performance capabilities. Some works on this topic can be found in literatures[1-5]..

DESIGN METHODOLOGY

Lego mindstorms line follower robot design

A line follower shown in Fig.1 is a mobile robot which is able to follow a visible line on a surface consisting of contrasting colours. To build and run the robot, the required hardware included; Lego EV3 brick, power supply, 2 large servo motors, a set of wheels, colour sensor, connector cables, beams, axles, bushes and pins. The EV3 brick formed part of the chassis, equipped with wheels. The servo motors are used to drive the two front wheels. Two rear small castor wheels supported the robot. The robot had a colour sensor mounted at the front end to identify the line. It is centered between the two front wheels, which are separated by a distance of 7.4 cm. It is designed to follow an oval track made of black electrical tape (18 mm wide) on a white surface.

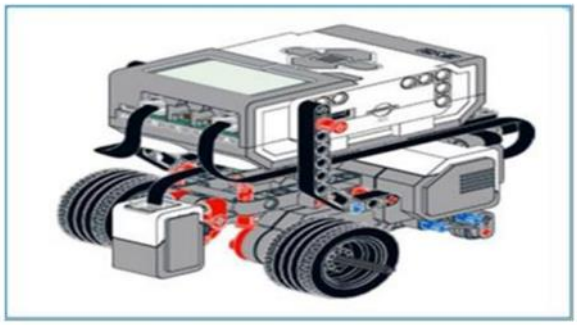

FIGURE 1. Line Following Robot

Study of Lego Mindstorms EV3 motor

Lego Mindstorms has not published the EV3 motor's electromechanical characteristics. Table 1 shows the proposed parameters used in this paper, while, Table 2 shows the operational specifications.

TABLE 1. Lego Mindstorms EV3 large Motor Characteristics

Motor Parameter	Unit	Value
Torque constant,	N.m/A	0.2
Back e.m.f constant,	V.s/rad	0.5
Armature resistance,	Ω	5
Armature inductance,	H	0.005
Viscous damping coefficient, B	N.m/rad.s	0.0006
Rotor inertia coefficient, J	N.m.	0.001

TABLE 2. Operational Specification

Nominal Voltage	7.2V or 9V
Rotation Speed at no load	160 – 170 rpm
Running Torque	0.20 N-m
Stall Torque	0.40 N-m

Fig.2 shows the motor model simulated using MATLAB Simulink.

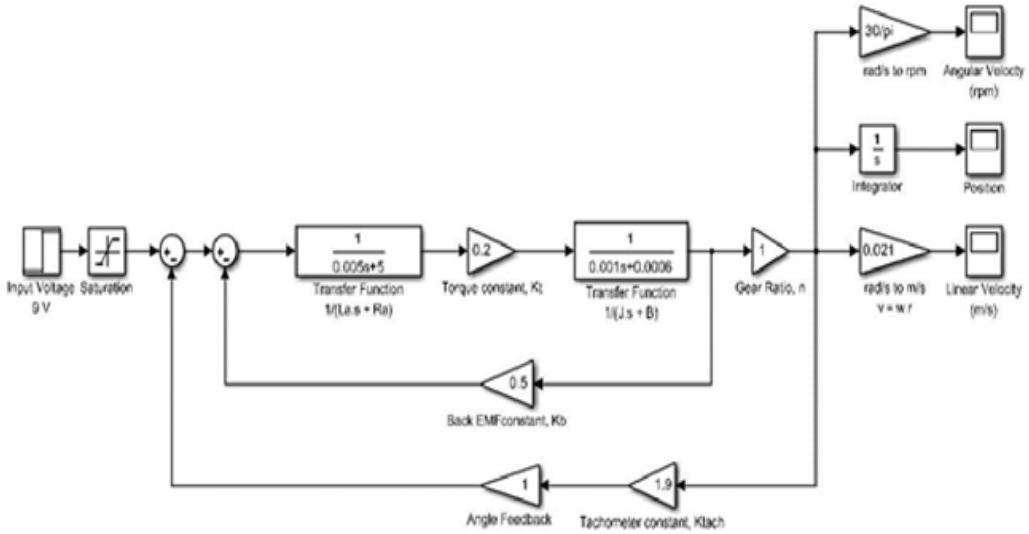

FIGURE 2. Motor Implementation on Simulink

Line following robot algorithms

Line following works by using the colour sensor (in reflected light intensity mode) to read the changes in the reflected light levels along the edge of a dark and light surface. The reflected light intensity is measured as a percentage from 0% (very low reflectivity) to 100% (very high reflectivity). More light is reflected from a white surface compared to the black surface. Depending on the light sensor value, the motors are directed to vary the speed.

In a program, white and black values are defined using a threshold value. Threshold is the average of the sensor value with the sensor on the black line and one found on the white area. Different measurements for black and white depend on factors such as the light level in the room, the robot' s battery level, and the type of surface used.

The light sensor will read the light value. Then the robot can be programmed such that if the sensor sees black, which is when the sensor value is less than the threshold, the robot should turn right, else it should turn left. The basic line following approach is shown in Fig.3, and can be summarized as follows:

1. The robot will be started. It will then be set to move forward. It will be made to steer right until it detects the line edge.

2. Once the sensor sees black, the robot will continue to go forward while turning left gradually.
3. Whenever the sensor will see white (i.e. the robot leaving the line), the robot will turn to the right until the sensor finds black again.
4. The sequence then will be repeated in a loop, unless the robot is stopped.

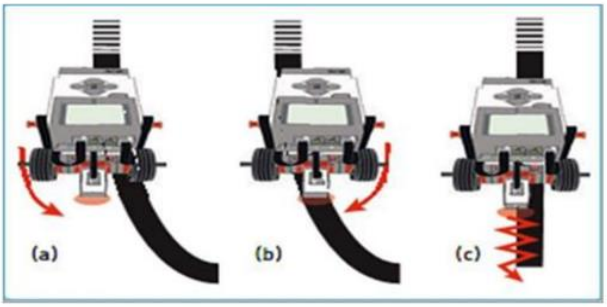

FIGURE 3. Basic Line Following approach

Digital controller design

A robot without a controller will oscillate a lot about the line, leading to more consumption of battery power, less speed and following the line less efficiently.

When designing a line following robot, the transient response specifications are defined as:

1. Rise time: It is how fast the robot will try to get back to the line after it has drifted off.
2. Overshoot: The distance past the line edge the robot will tend to go as it is responding to an error. 3-The amount of overshoot indicates the relative stability of the system.
3. Steady-state error: The offset from the line as the robot follows a long straight line.
4. Settling time: The time the LFR will take to settle down when it encounters a turn.

The performance criteria are stipulated as follows:

1. Constant speed of 0.1m/s to be maintained despite the presence of turns.
2. Steady-state error: Less than 2%
3. Settling time of less than 0.1 seconds
4. Overshoot (%) of less than 1.0
5. Finite phase margin

The robot controller to be designed is to be modified until the transient response met is satisfactory.

Digital controller design

The proposed controller is a Proportional-plus-Integral-plus-Derivative (PID) digital controller. The PID controller would control the position of the robot with quick response time and minimize the overshoot. The proportional part would determine the magnitude of turn required to correct the error sensed. The integral part would improve the steady state error (proportional offset) which increases while the robot is not on the line. The derivative part would measure the deviation from the path and minimize overshoot. It would reduce the oscillating effect about the line. The derivative control is used to provide anticipative action.

Implementation of line following control algorithm for lego mindstorms EV3 hardware

Fig.4 shows the Simulink line tracking program with PID controller, while Fig.5 shows EV3 software line following program with PID controller. Sensors and motors contain blocks that interface with the EV3 hardware. Actual speed values block uses the values from each motor encoder to calculate the position and velocity of the robot. Desired velocity takes the user-provided velocity (m/s) and converts it into the desired state values for the velocity controller. Desired light takes the color sensor's white and black values to choose an appropriate reference value for

the light. Velocity control has the PID controller implementation to control the forward velocity. Line tracking controller has the PID controller implementation to control the turning.

However, to download and run a line tracking Simulink model on the Lego Minfstorms EV3 robot, EV3 Wi-Fi Dongle or USB Ethernet Adaptor, and Wi-Fi Router are required to set up a network connection between EV3 brick and host computer.

The line following program is then written in EV3 software programming language. The black and white light intensity values are calibrated accordingly for the robot and the track. Using the provided USB cable, the program is downloaded and run on the robot. PID parameters(Kp, Ki, and Kd) tuning is done experimentally to achieve smoother line tracking.

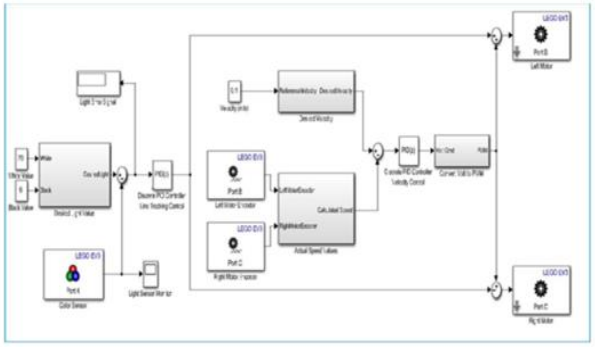

FIGURE 4. Simulink line tracking program with PID controller

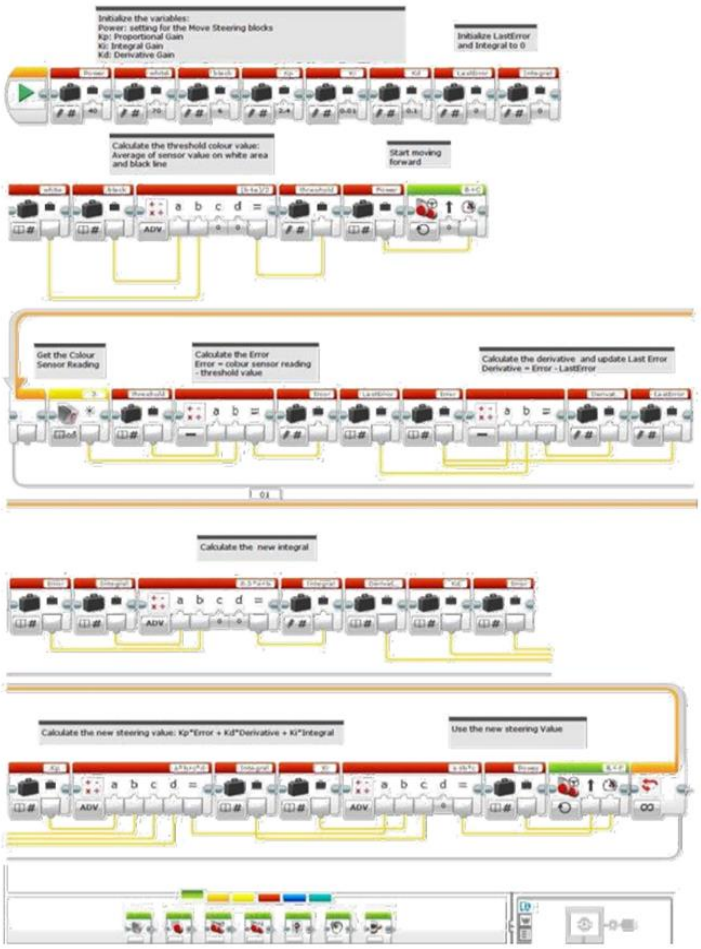

FIGURE 5. EV3 Software Line Following Program with PID Controller

SIMULATION RESULTS

EV3 large motor characteristics

Table 3 shows the EV3 motor load characteristics, from which the linear relationship between power level and EV3 large motor speed noticeable as shown in Fig.6. Also, from table 3, the rotation speed of the EV3 large motor is proportional to the input voltage.

TABLE 3. EV3 motor load characteristics.

Input Voltage	Torque	Rotation speed	Current	Mechanical power	Electrical power	Efficiency
4.5 V	17.3 N.cm	24 rpm	0.69 A	0.43 W	3.10 W	14 %
6.0 V	17.3 N.cm	51 rpm	0.69 A	0.92 W	4.14 W	22 %
7.5 V	17.3 N.cm	78rpm	0.69 A	1.41 W	5.17 W	27 %
9.0 V	17.3 N.cm	105 rpm	0.69 A	1.90 W	6.21 W	31 %
10.5 V	17.3 N.cm	132 rpm	0.69 A	2.39 W	7.24 W	33 %
12.0 V	17.3 N.cm	153 rpm	0.69 A	2.77 W	8.28 W	33 %

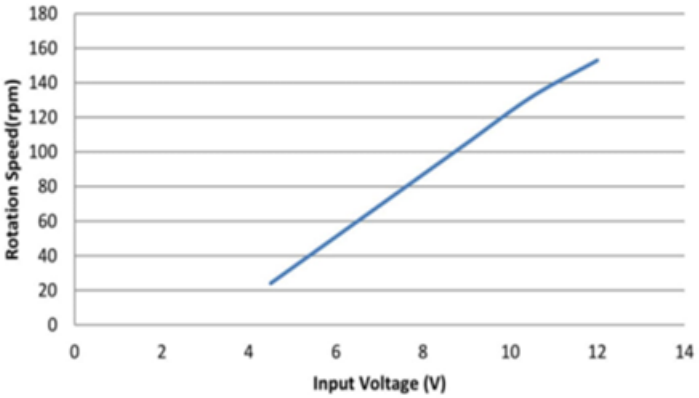

FIGURE 6. Graph of Rotation Speed Againts Applied Voltage

PID parameters tuning

Different values of PID parameters(Kp, Ki, Kd) are chosen in order to get the step response.

1. For Kp=1, Ki=0, Kd=0

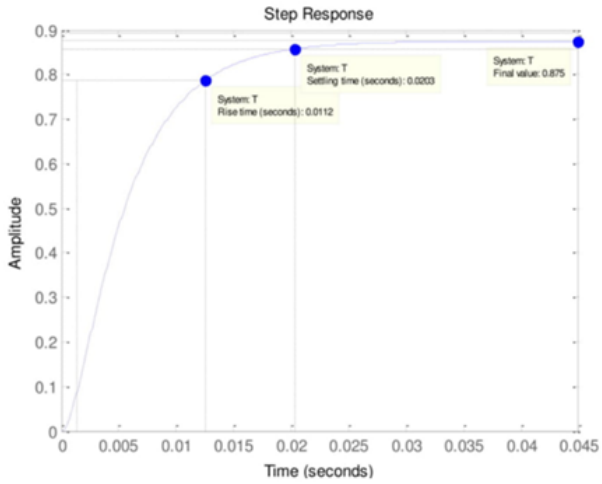

FIGURE 7. Step Response : $K_p = 1$

Observations:
Rise time = 0.0112 seconds
Settling time = 0.0203 seconds
Final value = 0.875

2. For Kp=5, Ki=0, Kd=0

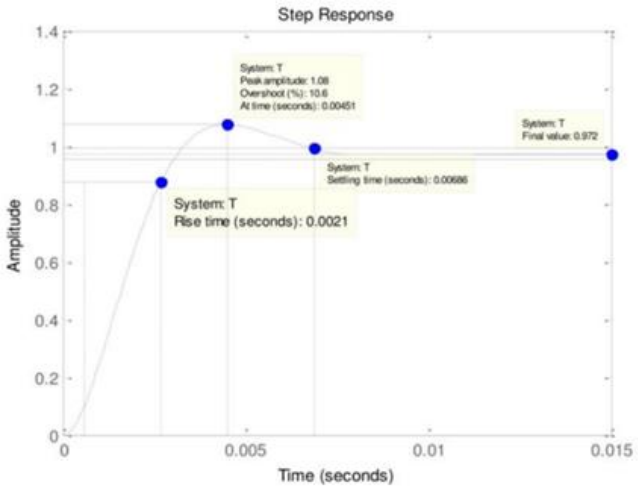

FIGURE 8. Step Response : $K_p = 5$

Observations:
Rise time = 0.0021 seconds
Settling time = 0.00686 seconds
Final value = 0.972
Overshoot (%) = 10.6
Peak amplitude = 1.08

3. For Kp=2.4, Ki=0, Kd=0

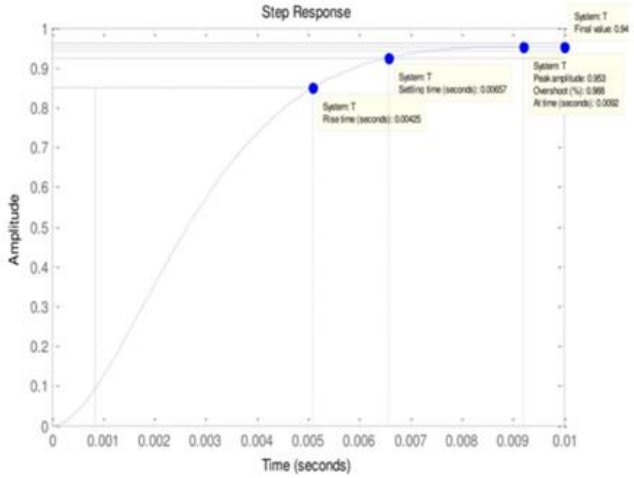

FIGURE 9. Step Response : K_p = 2.4

Observations:
Rise time = 0.00425 seconds
Settling time = 0.00657
Final value = 0.94
Overshoot (%) = 0.988
Peak amplitude = 0.953

4. For Kp=2.4, Ki=0.01, Kd=0

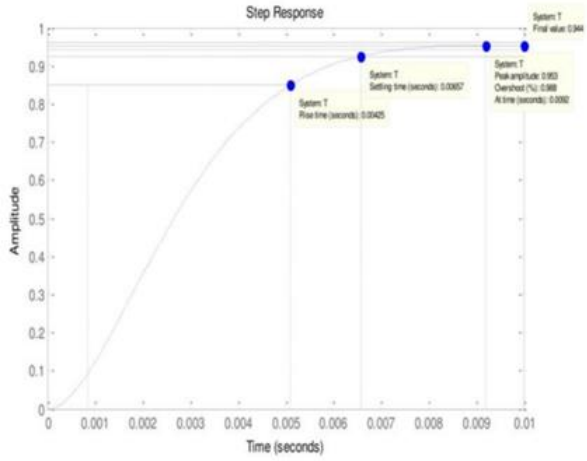

FIGURE 10. Step Response : K_p = 2.4, K_i = 0.01, K_d = 0

Observations:
Rise time = 0.00425 seconds
Settling time = 0.00657 seconds
Final value = 0.944
Overshoot (%) = 0.988
Peak amplitude = 0.988

5. For Kp=2.4, Ki=0.01, Kd=0.1

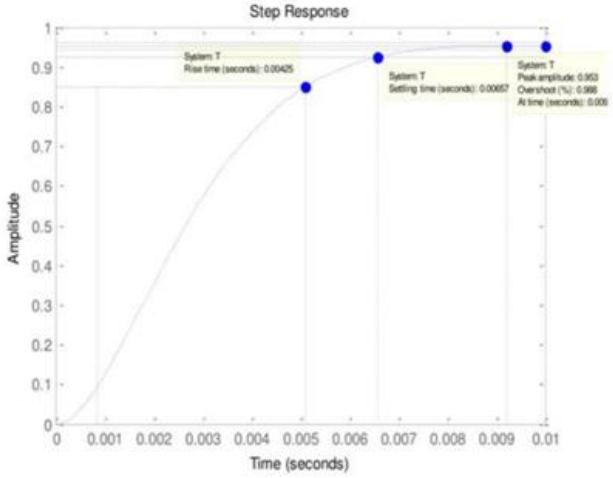

FIGURE 11. Step Response : K_p = 2.4, K_i = 0.01, K_d = 0.1

Observations:
Rise time = 0.00425 seconds
Settling time = 0.00657 seconds
Final value = 0.944
Overshoot (%) = 0.988
Peak amplitude = 0.953

Frequency response

Different values of PID parameters(Kp, Ki, Kd) are chosen in order to get the step response Frequency responses are obtained for different values of PID parameters.
1. For Kp=5, Ki=0, Kd=0

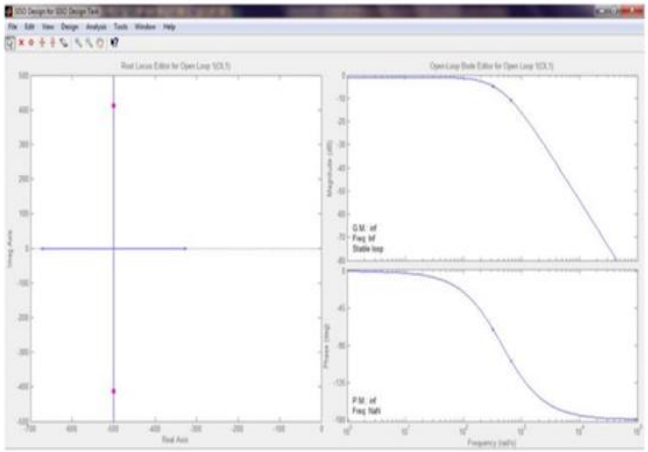

FIGURE 12. Various Frequency Plots for The Compensated System During Tuning (K_P = 5).

Observations

- The root locus exhibited complex closed loop poles.
- Both the phase and gain margin are infinite.
- The system is stable.

2- For Kp=2.4, Ki=0.01, Kd=0.1

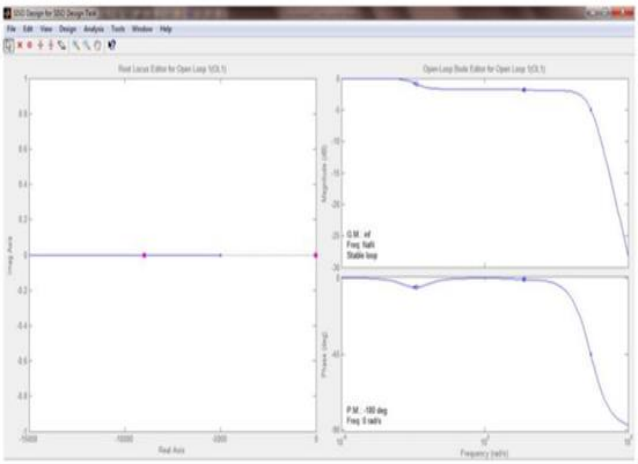

FIGURE 12. Various Frequency Plots for The Compensated System During Tuning (K_p = 2.4, K_i = 0.01, K_d = 0.1).

Observations

- The root locus closed-loop poles changed from complex to real.
- The system is still stable.
- The infinite gain margin showed inherent stability.

GENERAL ANALSIS

The effects of each of the controller parameters, K_p, K_i, and K_d on the line following the robot are summarized in Table 4.

TABLE 4. Effect of Increasing PID Parameters.

Parameter	Rise Time	Overshoot	Settling Time	Steady-state Error
K_p	Decrease	Increase	Small change	Decrease
K_i	Decrease	Increase	Increase	Eliminate
K_d	Small change	Decrease	Increase	No change

The difficulty of tuning increased with the number of parameters to be adjusted. To observe the response resulting from the tuning adjustments, it is necessary to wait several minutes. This made the tuning by trial-and-error a tedious and time-consuming task.

In practice, a mathematical model's stability is insufficient to guarantee acceptable system performance or even to guarantee the stability of the physical system that the model represented. This is because of the approximate nature of mathematical models.

The main problems associated with the implementation of digital control are related to the effects of quantization and sampling. The advantages of digital control outweigh its implementation problems for most of the applications.

CONCLUSION

A line following robot was designed and built using Lego Mindstorms EV3 components. Digital control algorithms were developed. The advantages and limitations of implementing digital control on different software were studied. The effectiveness of using a PID controller for optimum line tracking was demonstrated by inspecting the movement pattern of the robot while following the track. Kp, Ki and Kd were successfully determined by tuning to obtain the desired control response.

REFERENCES

1. M. Mutheke, "Digital control of a line following robot", Graduation Project, University of Nairobi, Kenya, 2015.
2. A. Pathak, " Line follower robot for industrial manufacturing process", International Journal of Engineering Inventions, Vol.6, Issue 10, PP. 10-17, 2017.
3. N. Chowdhury, "Algorithm for line follower robots to follow critical paths with a minimum number of sensors", International Journal of Computer, Vol.24, No.1, PP. 13-22, 2017.
4. P. Kumaresan, " Case study: A line following robot for hospital management", International Journal of Pure and Applied Mathematics, Vol.116, No.24, PP.529-537, 2017.
5. A. Attar, " Line follower and obstacle avoidance bot using Arduino", International Journal of Advanced Computational Engineering and Networking, Vol.5, Issue 4, PP. 18-21, 2017.

Effect of Hydroxyapatite Filler on Mechanical Properties of PE/HAp Composite as a Candidate for Bone Repair

Fitriyatul Qulub[1,a)], Inten Firdhausi Wardhani[1]

[1] *Department of Biomedical Engineering, Faculty of Science and Technology, Universitas Airlangga, Campus C, Surabaya 60115, Indonesia*

[a)] Corresponding author: fitriyatul.qulub@fst.unair.ac.id

Abstract. Polymer is one material that can be used as a fixation to repair fractured or broken bones. However, polymers are soft and ductile, so modifying them by adding hydroxyapatite as a filler is necessary. Polyethylene is a high-density polymer with more potent material properties to be utilized as a matrix. The PE-HAp composites were synthesized by compacting and heating the composition percentage of Hap 25%, 35% and 45%. Based on the characterization results using XRD, FTIR, and hardness test instruments, it is concluded that the addition of HAp composition results in better composite mechanical properties. The material properties are improving, increasing the hardness value (shore A) by 63 shore A. The hardness value increases because the composite properties are more compact, and the PE matrix physically binds the HAp filler. This is reinforced by XRD and FTIR characterization results, with no new compounds formed and no new molecular vibrational patterns in the FTIR spectrum.

ARTICLE INFO

Article history:

Received: 1 June 2023

Revised: 20 November 2023

Accepted: 21 November 2023

Available online 14 December 2023

Keywords:
PE-HAp Composite,
Bone Repair,
Biomaterials.

Cite this as:
Qulub, F., & Wardhani, I. F. Effect of Hydroxyapatite Filler on Mechanical Properties of PE/HAp Composite as a Candidate for Bone Repair. Indonesian Applied Physics Letters, 4(2). https://doi.org/10.20473/iapl.v4i2.48649

Indonesian Applied Physics Letters
e-ISSN: 2745-3502
DOI: 10.20473/iapl.v4i2.48649

INTRODUCTION

Research on developing polymer-based composites as biomaterials for prosthetics is growing along with the advancement of biomaterial technology. One of the applications of biomaterials in the medical field is bone substitution, which supports the body and protects the fracture area by maintaining its shape during healing.

Commercially, one of the materials that can be used as bone substitution is hydroxyapatite (HAp). Hydroxyapatite with the chemical formula $Ca_{10}(PO_4)_6(OH)_2$ is an example of powdered apatite. It is the main inorganic component in bones and teeth [1], but HAp has the limitation of being brittle so that it is easily broken. HAp must be modified by adding a polymer as a matrix to qualify as a bone substitute material. The material used as a matrix must have non-toxic, osteoconductive, biocompatible, biodegradable, and non-carcinogenic properties [2]. Polyethylene (PE) is a high-density polyethylene with more potent material properties that can be utilized as a matrix to manufacture bone-replacement biomaterial composites. In addition, PE is highly resistant to chemicals and is economically priced.

The synthesis of PE-HAp composites was carried out by compacting and heating methods, hoping to improve the hardness properties of the composites. In this study, the synthesis of modified PE-HAp composites with variations in HAp composition was carried out. The results of the synthesis of PE-HAp composites were characterized using XRD instruments for phase analysis, FTIR for functional groups in composites, and analysis of mechanical properties carried out by hardness tests.

This research aims to synthesize PE-HAp composites in the form of pellets and determine the mechanical properties and physical properties of PE-HAp composites.

METHODOLOGY

Tools And Materials

The equipment used included an analytical reader, compacting machine, furnace, Zwick shore A, X-ray diffraction (XRD) (Philips type Shimadzu 610), and FT-IR (Tensor 27). The materials used were hydroxyapatite and polyethylene granules (Mr PE = 15,000 g/mol).

Synthesis of PE-HAp composites

Synthesis of PE-HAp composite by compacting and heating method. PE and HAp with a total weight of 6 grams at a percentage of HAp of 25%, 35%, and 45% (w/w) and put into a square mould with a size of 15 cm × 15 cm and a thickness of about 0.5 mm. The mould was then inserted into a hot felting device at 180°C and pressed with an initial pressure of 50 kg cm-2 for 1 minute. The sample was then subjected to additional pressures of 100 kg cm^{-2} for 1 min and 120 kg cm^{-2} for 5 min, for a total time of 7 min. Afterwards, the samples were removed from the hot felts and transferred into the cold felts.

Characterization of PE-HAp composites

The synthesized PE-HAp composites were characterized using Zwick shore A for hardness test, XRD for phase analysis, and FTIR to analyze functional groups in PE-HAp composites.

RESULTS AND DISCUSSION

Synthesis of PE-HAp Composites

Synthesis of PE-HAp Composites by Compaction and Heating Method. The synthesis of PE-HAp composites was carried out by cold compaction method, with the percentage of Hap at 25%, 35%, and 45% (w/w). The compressed composite (felts) is brittle, and of low strength, so heating is carried out at 180oC to homogenize the PE-HAp composite and increase its mechanical strength. Composites are alloys of two or more substances that combine

physically and do not undergo chemical reactions between the substances. The synthesis of PE-HAp composites was carried out by hot felting and cold felting methods.

When the composite melts, the crystallinity of PE decreases [3] and has an irregular particle arrangement, resulting in a physical reaction with HAp. HAp can fill the amorphous particles of PE and physically bond to improve its mechanical properties.

Characterization of PE-HAp Composites

Shore A Hardness Test

The mechanical properties of PE-HAp composites determine the quality of the composite application. In this study, the effect of Hydroxyapatite composition on the mechanical properties of composites was studied. The hardness test using the Zwick Shore A tool can determine mechanical properties, so the hardness value is obtained, as shown in Figure 1.

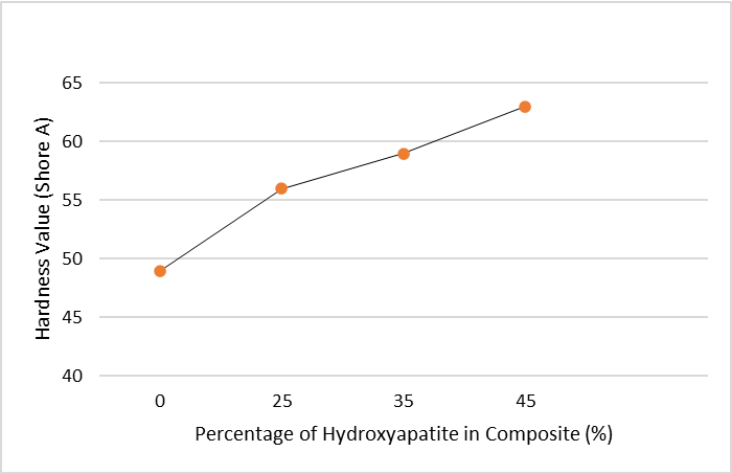

FIGURE 1. Hardness values of composites against HAp composition

The composition ratio of hydroxyapatite addition also influences the hardness value of the PE-HAp composite. The most excellent hardness value is at 45% HAp percentage of 63 shore A. In the 25% HAp percentage composition, there is a strong interaction between PE as a matrix and HAp as a filler, forming a more compact matrix

Phase Characterization with XRD

XRD characterization was used to analyze the phase and degree of crystallinity of PE-HAp composites before and after gamma radiation. Based on the diffractogram pattern in Figure 5 shows a specific phase for PE polymer at angles $2\theta = 19.4°$, 21.5°, and 23.95°. This is to the research of Kim et.al (2010) that the specific PE phase at $2\theta = 21.44°$, 23.83° and Jaggi et al. (2012) at $2\theta = 26$, 44° and 21.39°, 23.56° and 36.13° [4,5].

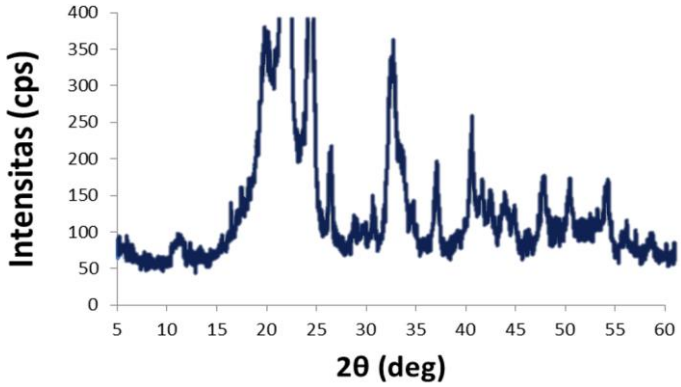

FIGURE 2. XRD spectra of PE-HAp

The specific diffractogram patterns of HAp (Figure 5) are at angles 2θ = 25.85º, 26.22º, 32.1º, 36.4º and 39.85º. This is by the Joint Committee Powder Diffraction Standards (JCPDS) database number 50-0584 for pure HAp at angles 2θ = 18.6º, 21.18º, 24.56º, 25.42º, 26.12º, 31.03º, 32.29º, and 36.44º.

Characterization of Function Groups with FT-IR

FTIR characterization aims to determine the functional groups in PE-HAp composites formed by the felt method. PE molecules have specific vibrations at wave numbers 2915, 2850, 1467 and 720 cm^{-1} [6], while the functional groups identified in HAP include phosphate groups (PO_4^{3-}) at wave numbers 1024-1092 cm^{-1}, carbonate groups (CO_3^{2-}) at wave numbers 1420 and 1456 cm^{-1}, and hydroxyl groups (OH^-) at wave numbers around 3576 and 632 cm^{-1} [7]. The vibrational bands of the synthesized PE-HAp composite are presented in Table 3.

TABLE 3. Vibrational bands synthesized on PE-HAp composites

Wavenumber (cm^{-1})	Vibration	Molecular
2913,05	Symmetry bendC-H	PE
2852,02	Asymmetry bendC-H	PE
1653,64	Asymmetry bend CO_3^{2-}	HAp
1470,55	Groove C=C	PE
1027,80	Asymmetry bend PO_4^{3-}	HAp
724,34	Bend $(CH_2)_n$	PE
641,12	Bend OH	HAp

FTIR spectra provide information on the nature of the reaction between PE-HAp composites. The FTIR spectra suggest that the HAp filler is physically bound to the PE matrix. This can be seen in the typical peaks of each HAp and PE spectra, and no new absorption bands were found as new molecules formed [8,9].

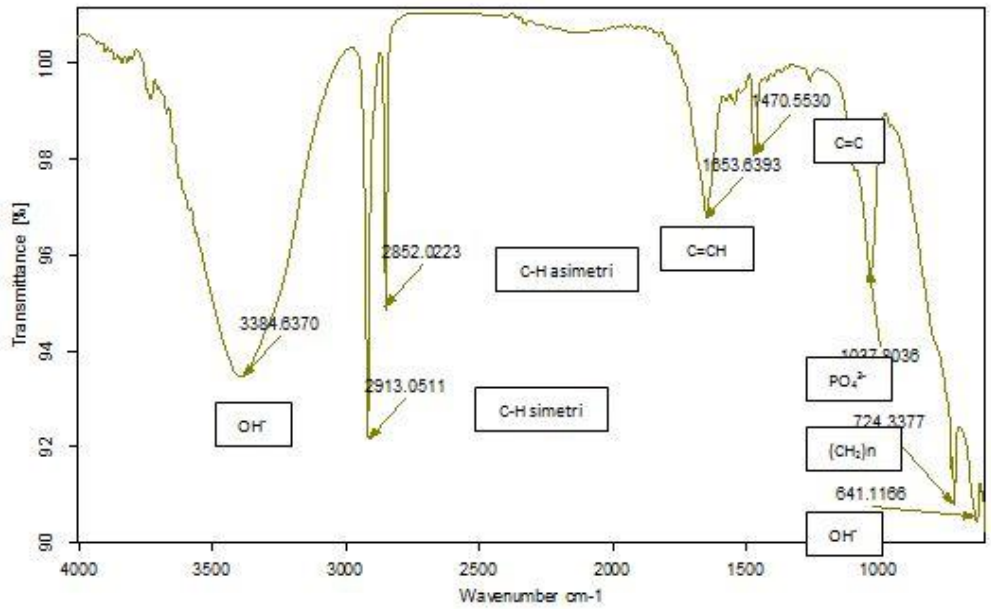

CONCLUSION

The synthesis of PE-HAp composites was carried out by hot compressing and heating methods. The percentage ratio of HAp is 25%, 35%, and 45% (w/w) to PE/HAp composite. The percentage of 45% has more complex material properties with a hardness value of 63 shore A. XRD diffractogram patterns of HAp 25.85º, 26.22º, 32.1º, 36.4º and 39.85º. The presence of HAp filler does not significantly affect the mechanical properties because the interaction of HAp filler with the PE matrix is a physical reaction.

REFERENCES

1. Kehoe S, 2008. Optimisation of Hydroxyapatite (HAp) for Orthopaedic Application via the Chemical Precipitation Technique [Thesis] School of Mechanical and Manufacturing Engineering. Dublin: Dublin City University.
2. Wang M. 2004. Bioactive Ceramic-Polymer Composites for Bone Replacement. Singapore: Nanyang Technological University. *Journal.* School of Mechanical and Production Engineering.
3. Kusumawati. 2012. Pengaruh Radiasi Gamma Terhadap Sifat HDPE untuk *Tibial Tray*. [*Skripsi*]. Yogyakarta: Sekolah Tinggi Teknologi Nuklir-BATAN.
4. Jaggi, H.S; Kumar, Y; Satapathy, B.K; Ray,A.R; dan Patnaik,A. 2012. Analytical interpretations of the structural and mechanical response of high-density polyethylene/hydroxyapatite biocomposites. Journal Materials and Design (36) 757–766
5. Kim, B.J; Byun, J.H dan Park, S.J. 2010. Effects of Graphenes/CNTs Co-reinforcement on Electrical and Mechanical Properties of HDPE Matrix Nanocomposites. Korea: Univ.Incheon 402-751. Dept. *Journal* of Chemistry, Inha. Vol.31, No.8.
6. Ilie & Setnescu. 2009. Radiation-Induced Aging Effects in Polymeric Cable Insulators at CERN. Compilation of the DSC and ATR-FTIR data on irradiated Cern Cables. European Organization For Nuclear Research Organisation Européenne Pour La Recherche Nucléaire. CERN TE –VSC.
7. Muntamah. 2011. Synthesis and characterization of hydroxyapatite from blood clam shells (Anadara granosa, sp) [Thesis]. Bogor: Graduate School, Bogor Agricultural University.